AD-A041 821 NAVAL RESEARCH LAB WASHINGTON D C F/G 13/2
THE MEASUREMENT OF OIL SPILL VOLUME BY A PASSIVE MICROWAVE IMAG--ETC(U)
MAY 77 B E TROY, J P HOLLINGER

UNCLASSIFIED NRL-MR-3515 NL

1 OF 1
ADA
041821

END
DATE
FILMED
8-77

NRL Memorandum Report 3515

The Measurement of Oil Spill Volume by a Passive Microwave Imager

BALLARD E. TROY, JR. and JAMES P. HOLLINGER

Advanced Space Sensing Applications Branch
Space Science Division

May 1977

NAVAL RESEARCH LABORATORY
Washington, D.C.

SECURITY CLASSIFICATION OF THIS PAGE (When Data Entered)

REPORT DOCUMENTATION PAGE

READ INSTRUCTIONS BEFORE COMPLETING FORM

1. REPORT NUMBER: NRL Memorandum Report 3515
2. GOVT ACCESSION NO.:
3. RECIPIENT'S CATALOG NUMBER:

4. TITLE (and Subtitle): THE MEASUREMENT OF OIL SPILL VOLUME BY A PASSIVE MICROWAVE IMAGER.

5. TYPE OF REPORT & PERIOD COVERED: Final report, on an NRL problem.

6. PERFORMING ORG. REPORT NUMBER:

7. AUTHOR(s): Ballard E. Troy, Jr. and James P. Hollinger

8. CONTRACT OR GRANT NUMBER(s):

9. PERFORMING ORGANIZATION NAME AND ADDRESS:
Naval Research Laboratory
Washington, D.C. 20375

10. PROGRAM ELEMENT, PROJECT, TASK AREA & WORK UNIT NUMBERS:
NRL Problem G01-08
DOT-USCG 2-21881

11. CONTROLLING OFFICE NAME AND ADDRESS:
Department of Transportation
U.S. Coast Guard
Washington, D.C. 20590

12. REPORT DATE: May 1977

13. NUMBER OF PAGES: 67 (12) 66 p.

14. MONITORING AGENCY NAME & ADDRESS (if different from Controlling Office): (14) NRL-MR-3515

15. SECURITY CLASS. (of this report): UNCLASSIFIED

15a. DECLASSIFICATION/DOWNGRADING SCHEDULE:

16. DISTRIBUTION STATEMENT (of this Report)

Approved for public release; distribution unlimited.

17. DISTRIBUTION STATEMENT (of the abstract entered in Block 20, if different from Report)

18. SUPPLEMENTARY NOTES

19. KEY WORDS (Continue on reverse side if necessary and identify by block number)

Water pollution
Oil pollution
Oil slick thickness
Oil slick volume
Oil slick spreading
Oil slick detection
Remote sensing
Passive microwave radiometry
Microwave imagery

20. ABSTRACT (Continue on reverse side if necessary and identify by block number)

An airbirne passive microwave system has been developed and used in a test program to detect a marine oil spill and to determine its thickness and volume. A controlled spill of 2040 liters (538 gallons) of No. 2 fuel oil was conducted from a Coast Guard vessel 20 miles off the Virginia shore. Microwave images of the spill were obtained at both 22.4 and 31.0 GHz on five consecutive aircraft passes over the visible oil slick. Wind and weather conditions were moderate during the test.

(Continues)

20. Abstract (Continued)

The microwave images were processed on a computer and shown on a color television display system. These color images revealed a small region of relatively thick oil, surrounded by a larger region of much thinner oil, in agreement with results from an earlier program. The thin oil region corresponded to the visible oil slick and showed up clearly in the color images against the unpolluted open sea. It is thus possible to outline the entire visible slick and to locate the thick oil regions within it by means of a microwave image. Maximum oil thickness was approximately 0.6 mm in the thick region which was located on the downwind side of the visible slick. The oil spill volume was determined by integrating the oil thickness over area in the computer.

Each microwave image of the spill was made in the few seconds necessary for the aircraft to pass over the spill. This rapid data-taking capability is a significant improvement over the earlier developmental program which used fixed downward-looking radiometers, and required approximately one hour and a dozen aircraft passes to gather the data necessary to reconstruct a microwave picture of the slick. Therefore, the development of the imager and the progress in analysis of the imager data represent a large step toward an airborne system for making real-time determination of oil spill volume.

CONTENTS

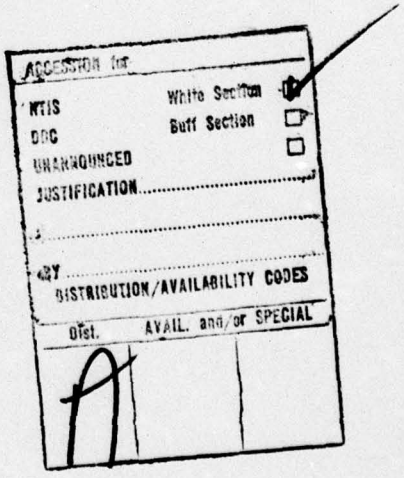

THE MEASUREMENT OF OIL SPILL VOLUME BY A PASSIVE MICROWAVE IMAGER

INTRODUCTION

The Naval Research Laboratory and the U. S. Coast Guard have developed a multifrequency microwave radiometric technique for the remote quantification of oil spills from aircraft (1), (2). This technique arises because the apparent microwave brightness temperature of an oil-covered sea surface is enhanced compared to that of the adjacent unpolluted sea by an amount which depends upon the oil film thickness. Further, oil spills do not spread uniformly nor without limit but instead thick regions are formed which comprise the bulk of the oil. The development program demonstrated that the thick regions can be located and their thickness determined with the use of microwave sensors. The film thickness along with the areal extent allows the volume of the slick to be estimated. A knowledge of the volume of oil is essential for litigation and damage claims resulting from major oil spills as well as for assessing the impact of the spill on marine life and environment. Perhaps most important, a knowledge of the oil distribution and the location of those regions containing the heaviest concentration of oil enables the most effective confinement, control, and clean up of the oil.

The development program included aircraft-borne measurements of fifteen controlled marine oil spills of from 760 to 2400 liters of either No. 2 fuel oil or No. 4 or No. 6 crude oil. The microwave measurements of the oil spills of each

Note: Manuscript submitted May 2, 1977.

oil type showed very similar results. Each slick formed an identifiable region with film thicknesses of a millimeter or more and containing the majority of oil which was surrounded by a very much larger and thinner slick which contained very little of the oil. In general the thick region contained more than 90 percent of the oil in less than 10 percent of the area of the visible slick. It was always possible to locate and delineate the thick region solely from the microwave observations. The total volume of oil present derived from the microwave measurements was within about 25 percent of the volume of oil spilled.

The airborne measurements were made with the microwave radiometers fixed in position to view directly below the aircraft. This technique necessitated repeated aircraft passes back and forth over the spill to obtain microwave measurements of the entire spill area. Photographs were taken during each pass over the slick and were used after the flight to determine the relative position of the passes over the slick. The microwave data from all of the passes were then combined to obtain a microwave brightness temperature map of the slick, from which oil film thicknesses contours were determined. The thickness contours were integrated over the slick to obtain oil spill volume. Although these measurements demonstrated the potential and feasibility of the microwave technique for oil spill quantification, the experimental procedure was time consuming and required post-flight data analysis and interpretation. A practical, operational airborne system would have to provide rapid measurement and evaluation of the spill area. Such a system must be capable of viewing a significant portion of the slick in a single aircraft pass over the spill and be able to perform the necessary computations with the measurements to display the oil thickness contours and oil volume in real-time or near real-time aboard the aircraft.

The Naval Research Laboratory has recently developed an airborne passive microwave scanning system capable of obtaining dual-frequency microwave brightness temperature images along a 64 degree wide field of view centered on the aircraft ground track (3). This scanning system has been used in a new progam with the Coast Guard to significantly improve the capability of measuring oil spill volume by microwave techniques. The objective of the present investigation is twofold: (1) to develop the methodology to allow real-time or near real-time on-board computation of oil slick thickness and slick volume using one or more microwave radiometric sensors, and (2) to use the new microwave scanning system to evaluate the real-time or near real-time oil thickness/volume capabilities of an airborne dual frequency scanning system and to test the methodology and algorithms for oil thickness/volume computation. To accomplish this objective, the Naval Research Laboratory, in conjunction with the U. S. Coast Guard, conducted a flight test of the microwave imaging system over two controlled oil spills on 25 September 1975, and subsequently developed the methodology and computer programs to analyze these data. The microwave system provided real-time images of the microwave brightness temperature of the oil spill on an on-board monitor. The conversion of these data to oil film thickness contours and determination of oil volume was performed by post-flight computer analysis and display. However, the post-flight computations could have been done in real-time on the aircraft using the same reduction algorithms had a suitable computer been aboard the aircraft. Therefore, the present investigation constitutes a test of a real-time operational system.

This report describes the dual-frequency imaging system as used in the test flight, the controlled oil spill test measurements, and the data reduction algorithms, analysis,

and the results of the tests. This investigation, the techniques developed, and the results from it verify the value and capability of a dual-frequency microwave imaging system to locate, delineate, and quantify marine oil spills on a real-time operational basis.

MICROWAVE IMAGING SYSTEM DESCRIPTION

The passive microwave imaging system has been discussed in detail previously (3) and only the features relevant to this investigation will be briefly described here.

There are three main parts to the imaging system: the data acquisition unit, located in the aircraft passenger compartment, and the oscillating mirror and radiometer, located in the aircraft bay beneath the passenger area. Each of these three units is self contained and may be operated and controlled separately. This design permits different antenna/radiometer combinations to be easily and quickly interchanged. Thus, observational parameters such as frequency, polarization and beamwidth can be readily varied. In addition, it allows a pre-existing inventory of radiometers to be used as imagers.

A sketch of the configuration is given in Figure 1. The radiometer antenna electrical axis and the rotational axis of the mirror are aligned with the keel of the aircraft. The mirror is scanned at a constant angular rate in a direction perpendicular to the keel, generating a sawtooth or zigzag raster over the ground with aircraft motion. The uniform rate zigzag scan is preferred over the more easily implemented sinusoidal scan because the time required to scan one resolution cell is constant over the scan width, whereas the sinusoidal scan moves at a $\pi/2$ greater rate at the center of the scan, where optimum measurement is desired, and more slowly near the edges of the scan. In addition the

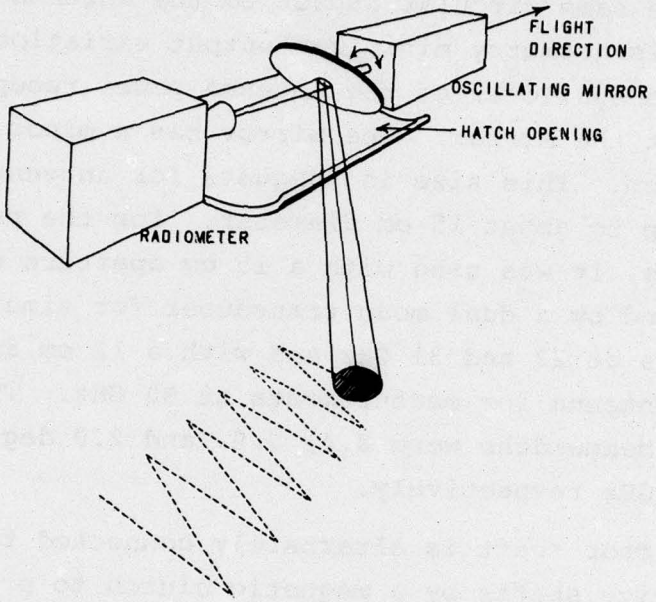

Fig. 1 — A sketch of the imager configuration. The oscillating mirror scans the reception pattern of the antenna/radiometer back and forth, forming a zigzag track across the ground with aircraft motion.

uniform rate zigzag scan simplifies data display and processing.

The mirror is elliptically shaped and mounted at an angle of 45 degrees to its rotational axis. Thus the mirror projects the same circular aspect to the antenna at all scan angles. This geometry minimizes output variations with scan angle due to spillover of the antenna power reception pattern past the mirror. The mirror has a minor axis dimension of 20 cm. This size is adequate for antennas with apertures up to about 15 cm diameter. For the present observations, it was used with a 15 cm aperture corrugated horn followed by a dual mode transducer for simultaneous measurements at 22 and 31 GHz and with a 12 cm aperture horn-lens antenna for measurements at 90 GHz. The resultant half-power beamwidths were 8.4, 7.9, and 2.0 degrees at 22, 31, and 90 GHz respectively.

The mirror shaft is alternately connected to contrarotating drive shafts by a magnetic clutch to produce the oscillating motion. The contrarotating drives are obtained from a common motor driven shaft by using gear to gear coupling for one sense of rotation and pulley to pulley coupling for the opposite sense of rotation. Only the thin magnetic clutch plate, mirror shaft and mirror reverse direction, minimizing the inertia to be overcome by the drive. Since the drive power required is highest during the very short time when the rotation is reversed, a flywheel is used to store energy during the remainder of the cycle and only a relatively small electric drive motor is required. The mirror can be scanned at any constant angle rate up to a maximum of 640 degrees/second and it reverses direction in less than 1 millisecond. The scan width is 64 degrees resulting in a maximum of 10 scan lines/second.

When the imager is operated at the single frequency, of

90 GHz, the radiometer output is passed through a low-pass filter, sampled at one degree intervals along the scan, digitized with 12-bit precision and stored in core memory. When the system is used to obtain images at 22 and 31 GHz simultaneously, one output of the transducer is received at 22 GHz and the other at 31 GHz. The outputs from the two radiometers are filtered appropriate to the sampling rate and alternately connected to the input of the data acquisition unit by an analog switch. The switching is performed each degree along the scan in synchronism with the mirror drive. This results in the output of one radiometer being sampled and stored at even degree intervals and the other at odd degrees. The two sets of data are later unfolded during computer processing and the two images presented separately. The sample commands are derived from a shaft encoder driven from the mirror axis, and the low pass filter is selectable such that the cut-off frequency is less than one-half the sample frequency. Blocks of digitized radiometer data composed of the most recent 128 scan lines along with the housekeeping, aircraft and radiometer calibration data necessary for processing are recorded periodically on a 9-track magnetic tape. The most recent 100 scan lines are continually displayed in real time on an onboard oscilloscope monitor. A replay mode exists so that previously recorded 128 line blocks of data may be recalled from the magnetic tape and displayed on the monitor. Recall can be done during non-data taking lulls in flight, or after the flight for initial editing of the data.

OIL SPILL MEASUREMENTS

Two controlled oil spills were conducted on 25 September 1975; one in the morning and the other in the afternoon. Both spills were made from the USCGC CHEROKEE. All phases of each spill including ship operation, dispensing of the

oil and the collecting of ground truth were managed by the U. S. Coast Guard. The airborne imaging measurements were made using the NASA-Wallops C-54 aircraft. The morning spill was 2040 liters (538 gallons) of No. 2 marine diesel fuel, and the microwave measurements were taken with the imager at 22 GHz and 31 GHz in the dual frequency mode. Photographs of the spill were made by both a 35 mm frame camera and a 35 mm continuous image slit camera, each of which had approximately the same field of view as the imager. Weather conditions, monitored by the U. S. Coast Guard during the spills, are shown in Table 1. The C-54 made 14 passes over the ship and/or spill in a racetrack flight pattern, passing the target area approximately once every seven minutes in the upwind direction at an altitude of 150 meters. The CHEROKEE was in the field of view and was seen on the imager monitor several times in early passes; oil spilling occurred during passes 6 and 7. After the ship moved away from the oil, microwave images of the spill alone were acquired on passes 10 through 14. Two more passes were made at 460 meter altitude for photographic purposes, after which data-taking ceased.

The procedure for spilling the oil was similar to that followed during the rough-sea oil spills of March 1973 - February 1974 (2): oil was pumped directly from the CHEROKEE's stern, after which the ship moved away from the spill. This method did not result in an undisturbed point spill during the rough sea tests, but rather resulted in the thick region of the spill being stretched out and broken-up, especially in high winds. Point spills have only been achieved in the calm sea tests of 1971-72, when the spills were conducted from small rubber boats (2). Since the wind during the 25 September spills was always 10 knots or greater, a good point spill was not to be expected, and the results of the data analysis bear out this expectation. The oil was not

TABLE 1.

WEATHER OBSERVATIONS FOR

25 SEPTEMBER 1975

TIME	CLOUD COVER	VISI-BILITY	WIND	DRY TEMP	WET TEMP	PRES-SURE	SEA TEMP	SWELL
1130	3/10	13 km	110/12 kts	25.0°C	23.5°C	30.18	22.8°C	1.2 m
1200	4/10	13 km	130/10 kts	25.0°C	23.5°C	30.18	22.8°C	.9 m
1300	5/10	13 km	140/13 kts	24.9°C	23.3°C	30.17	22.8°C	.9 m
1400	6/10	13 km	130/11 kts	26.5°C	23.5°C	30.16	22.6°C	.6 m
1500	6/10	13 km	130/10 kts	24.5°C	23.0°C	30.16	22.5°C	.6 m
1600	5/10	13 km	130/11 kts	24.5°C	23.5°C	30.15	22.5°C	.9 m

GENERAL COMMENTS

Test Position: 37-06.5N, 75-21.0W

1152 COMMENCED SPILL #1
1200 COMPLETED SPILL #1, 538 gallons of #2 marine diesel fuel
1520 COMMENCED SPILL #2
1527 COMPLETED SPILL #2, 313 gallons, #2 diesel

Oil formed an extremely thin slick making ground truth sampling and thickness measurement impossible.

dyed, as in some previous spills, so that the thick region could not be located visually during the observations or later in the photographs.

After the morning spill, the C-54 returned to Wallops Island, the 22/31 GHz dual frequency radiometer was replaced by the 90 GHz radiometer, and the C-54 proceeded to the test site for the afternoon spill. A test procedure similar to that of the morning spill was followed: twelve passes were made over the test area, during which 1185 liters (313 gallons) of No. 2 diesel oil were dumped. The aircraft altitude was 460 meters on the first nine passes and 230 meters on the last three. Unfortunately, the afternoon spill was not seen on the imager monitor in flight, nor was it detected later when color microwave images were produced during data analysis at NRL. Data kept onboard the CHEROKEE while the oil was dumped show that the oil pumping rate was considerably slower during the afternoon spill than during the morining spill, and shipboard observers report that the afternoon spill was more spread out and broken up than was the morning spill. It is presumed that the slower dumping rate, smaller volume of oil, and greater drift, together, resulted in the oil being distributed in an irregular fashion over a very large area so that it was everywhere too thin for detection. This contention is supported by the difficulty that the Coast Guard had in making a direct measurement of the slick thickness, finding that the "oil formed an extremely thin slick making thickness measurement impossible." Therefore, the results covered later in this report are all derived from the 22/31 GHz data taken during the morning flight.

DATA ANALYSIS AND RESULTS

The overall purpose of the oil spill program covered in this report is to develop the ability for real-time or near

real-time determination of oil slick thickness and volume by remote microwave methods. In the previous test program using fixed airborne radiometers (2), the necessary relations for data analysis were developed and it was demonstrated that oil spill volume could be determined by passive microwave measurements. In addition, the microwave imager has been successfully tested in an unrelated program (3). Therefore, the problem of real-time oil volume determination reduces to combining the imager's rapid data-taking ability with the previously proved calculation methods for use on a high-speed computer.

Figure 2 outlines the method for converting the microwave data into an oil volume measurement. For computer software development, the computation can be broken down into four parts, which will be dicussed separately:

(a) raw microwave data → antenna temperature array,

(b) antenna temperature → brightness temperature increase ΔT_b due to oil film,

(c) ΔT_b → oil film thickness, and

(d) integration of oil thickness → oil volume.

The computer programming for step (a) had been developed prior to the 25 September flights to analyze imager data taken in previous flights; a detailed description of the analysis routine for single frequency operation along with examples of 90 GHz imagery is given in reference (3). Data are taken in 64 x 128 arrays, each array comprising one microwave image. For dual frequency operation, the 22 GHz and 31 GHz outputs are sampled alternately, so that one full array contains two separate 32 x 128 arrays in checkerboard fashion to provide simultaneous images. These arrays are subsequently separated, and processed individually by computer.

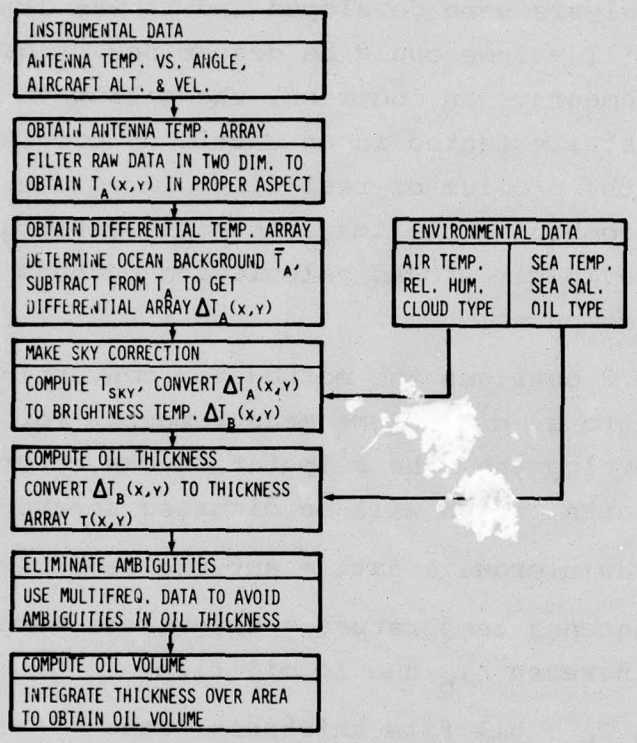

Fig. 2 — Major steps in the analysis routine to convert raw data into a determination of oil volume

Spurious isolated data values resulting from tape dropouts or other false "glitches" are found and eliminated, and the data values are converted to antenna temperatures using values from an internal reference and calibration sequence performed between passes over the slick. The locations on the earth's surface corresponding to the individual antenna temperature values comprise a two-dimensional grid of points, which is not regular, since the data were sampled at equal angle intervals, nor necessarily in the proper aspect ratio, depending upon the actual velocity/altitude ratio of the aircraft during that particular pass. Therefore a new set of locations is calculated to give a proper aspect ratio, square grid by interpolating within the bounds of the previous points with an appropriate sinc function. This process also provides filtering in two dimensions to remove noise at spatial frequencies beyond the reception capabilities of the equipment. The resulting antenna temperature array is then ready to be transferred from magnetic tape onto an NRL-developed display system for visual presentation (4).

Figure 3 shows an example of a processed 22 GHz image as seen on the display. The image, derived from a subset of the full 32 x 128 raw data array, represents a 29 x 29 array of filtered antenna temperature values. Before being presented on the display system, which has a 512 x 512 pixel capacity, the individual elements of the 29 x 29 array are expanded and smoothed. This procedure results in better visual perception of the image than the usual "confetti" method of depiction (3), (5). Different colors in the image correspond to different values of antenna temperature, as shown in the color bar at the bottom of the figure. The bright warm area in the center of the image is the CHEROKEE, seen here during pass No. 8; about five minutes after oil dumping had ceased. The maximum temperature measured in the

Fig. 3 — A 22-GHz microwave image of the CHEROKEE after oil dumping had ceased. The bright spot in the center is the CHEROKEE; the yellow area at the top is part of the oil slick.

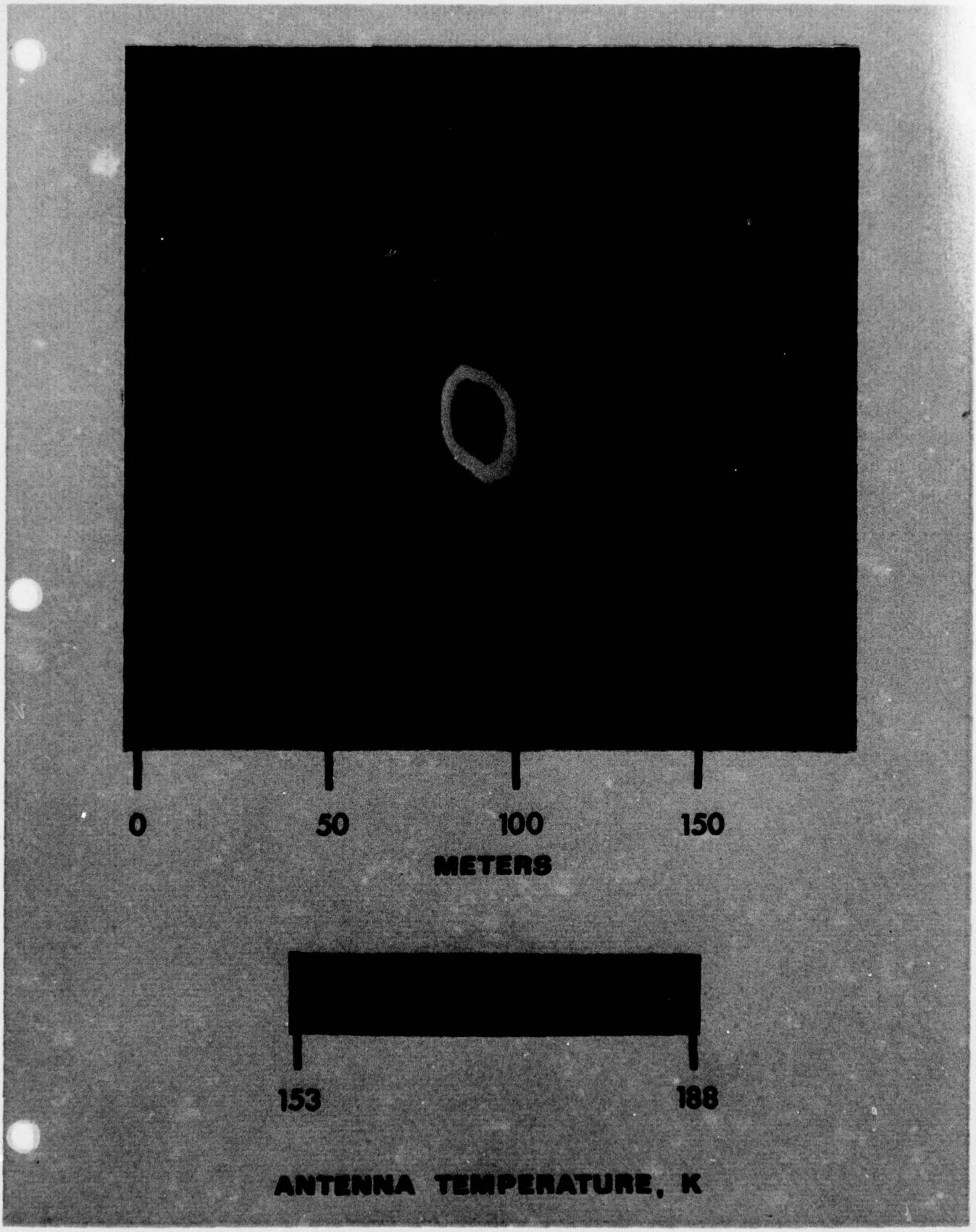
0
50
100
150
METERS
153
188
ANTENNA TEMPERATURE, K

warm area is 186 K, whereas the surrounding ocean water averages 168 K. Ordinarily, a metal ship would appear colder than the ocean since the metal emits very little microwave radiation and thus the signal received from it consists primarily of relatively cold sky radiation from above. But a large part of the CHEROKEE's deck was covered with wooden planking, with a high microwave emissivity, causing the ship to have a warm microwave signature. The bright yellow area at the top of the microwave image is the edge of the thick region of the oil slick, most of which is off the image. Notice the elongated similar yellow area at the CHEROKEE's stern, which is also due to thick oil. The antenna temperature of the yellow areas is approximately 173-175 K, and agrees with the antenna temperatures (seen on later passes) for the thick regions of oil. By the time pass 8 was made the CHEROKEE had begun to move away from the main part of the oil spill, but Figure 3 indicates that it had inadvertently pulled some of the oil along with it. This apparent breaking apart of the slick is consistent with the expectation that the dumping method employed would not yield a good point spill.

Photographs taken on pass 10 show that the CHEROKEE had separated completely from the visible slick, which had spread along the windward direction to a length of 500 meters. Microwave images of the isolated thick oil region were successfully taken on five consecutive passes, beginning with pass 10 and ending with pass 14. Figure 4 shows a microwave picture of the visibile slick and the open sea on each end of the slick, as seen on pass 10. This picture is composed of two consecutive unfiltered 22 GHz images, and corresponds to an area of 180 meters width and 1600 meters length. Presentation of the raw data images in this manner allows the display of a larger area than could be shown in a filtered image, such as Figure 3. Since this image has

Fig. 4 — A composite 22 HGz unprocessed image of the oil slick area on pass 10. Distance is compressed in the horizontal direction. The bright spot in the visible slick is the thick oil region; the other bright spot is the stern of the CHEROKEE.

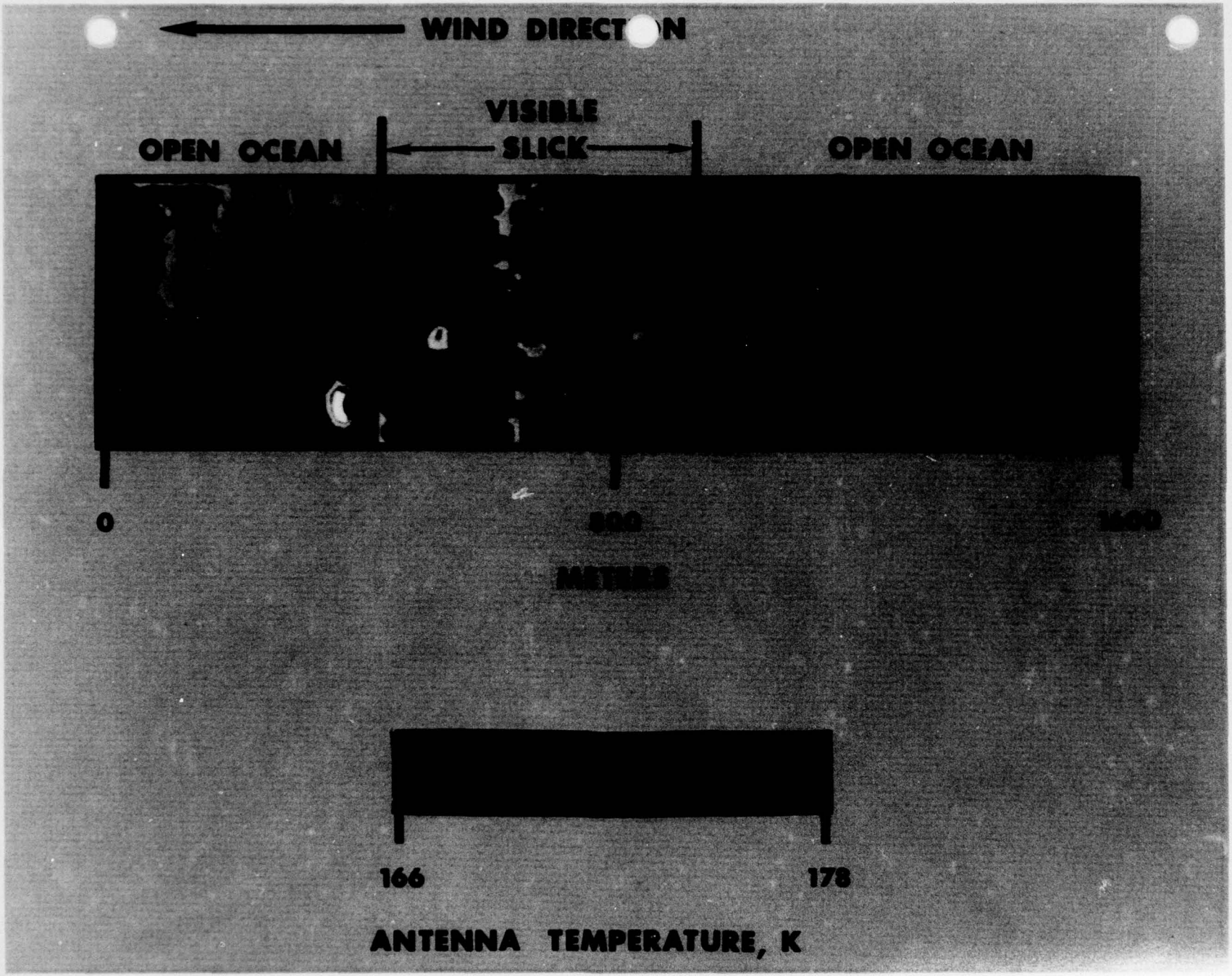
WIND DIRECTION
VISIBLE
OPEN OCEAN
SLICK
OPEN OCEAN
0
METERS
166
178
ANTENNA TEMPERATURE, K

not been processed to provide the proper aspect ratio, the horizontal scale is compressed by about a factor of two with respect to the vertical scale. The microwave antenna temperature range is 166-178 K, with blue being the coolest and yellow the warmest. The large blue area in the center of the picture is the visible slick, or the area of very thin film. To the left and right of the visible slick is open ocean, represented by the warmer red areas. This antenna temperature depression between the open sea and the thin oil film is in the opposite direction to the temperature increase caused by the thick oil and is a result of wind action. The wind creates capillary waves, which increase the antenna temperature of the ocean surface. A thin film of oil on the ocean damps the capillary waves, reducing the wind effect and causing an antenna temperature difference between the oil slick and the open sea, such as seen here. The central bright spot at the left end of the blue area, or visible slick, is the region of thick oil. Notice that the thick oil area is much smaller than the visible slick and that is is located on the downwind side of the visible slick. All of this information about the distribution of oil within the slick and the effect of wind on the slick confirms results from the earlier test program (1,2), but the data presented in Figure 4 represents the first time that such information could be gathered in a single aircraft pass over the slick.

The other bright spot in Figure 4, located in the red (open ocean) area, is the stern of the CHEROKEE. It is apparent that the open sea/oil slick boundary lies to the right of the ship, so that the microwave data agrees with the photographic result that the CHEROKEE has separated from the slick. In Figure 5, the antenna temperature is plotted versus distance along a left-to-right cut through the center of the oil slick shown in Figure 4. The dashed line

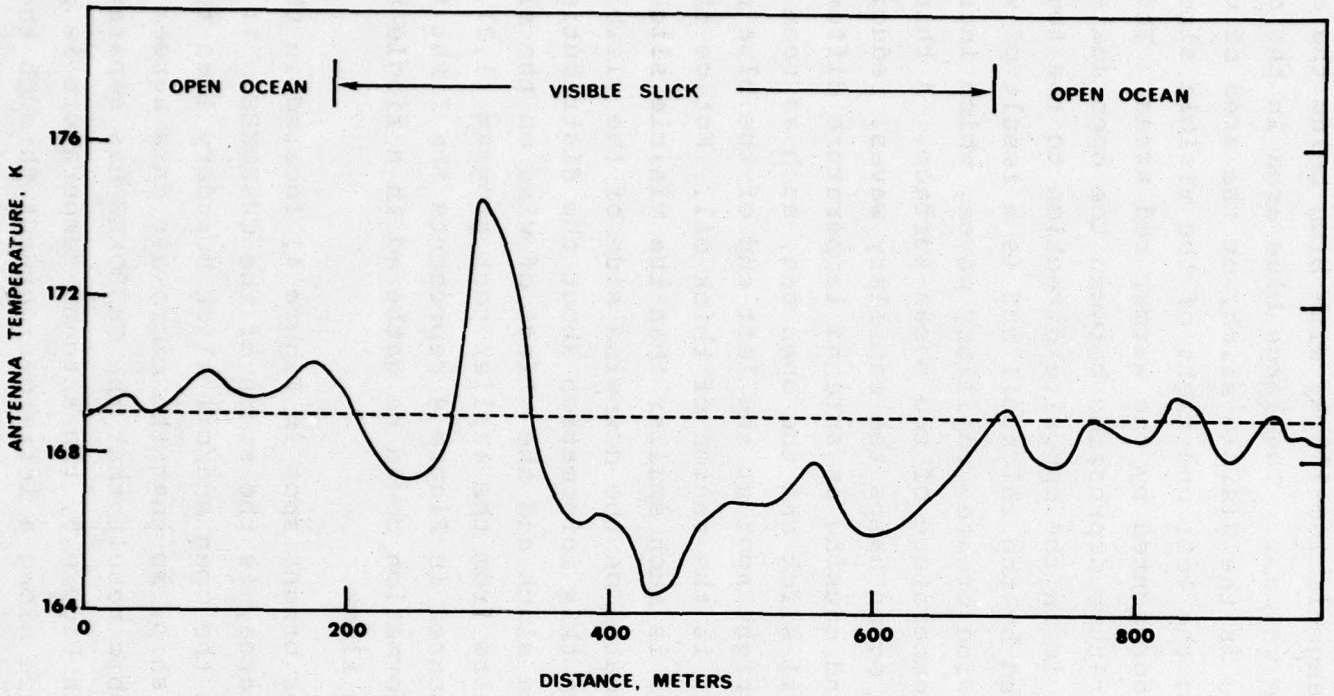

Fig. 5 — Antenna temperature vs. distance for a left-to-right cut through the center of Fig. 4. The peak in the visible slick is the thick oil region, and the horizontal dashed line is the average ocean antenna temperature of 169 K.

represents the average open ocean temperature of 169 K. Within the visible slick, the projection above 169 K is the thick oil region, i.e. the bright spot in Figure 4. The other portion of the visible slick in Figure 5, where the antenna temperature is less that 169 K, represents the region of thin oil, or the blue area in Figure 4. There is a depression of approximately 2 K in the thin oil region, in rough agreement with previous results for oil spills in similar wind conditions (2).

To show the oil distribution in pass 10 in greater detail, the region of thick oil in Figure 4 is filtered and put in the correct aspect ratio, and is displayed in Figure 6. The antenna temperatures are depicted as contours, each grey level representing a temperature differential of 2 K. The bright spot in the center of the image is the oil slick. Maximum antenna temperature in the center of the slick is 176 K; the surrounding sea averages 169 K. Notice that the microwave temperature of the ship (Figure 3) is greater than that of the oil, so that the ship is unlikely to be mistaken for oil on the microwave images. The size of the image is 180 by 180 meters, and the thick portion of the slick is approximately 60 meters wide.

Of the five passes (passes 10-14) in which microwave images of the thick region of the slick were obtained, the aircraft was slightly off course on two (passes 11 and 12), so that part of the thick region was off the image. The 22 GHz images for the well-centered passes 13 and 14 are shown in Figures 7 and 8. It is interesting that in all three images (passes 10, 13 and 14) the shape of the thick region is moderately stable, even though the images are separated in time by over a half-hour. This stability is in agreement with earlier results (2) in which it was found that the thick region of the slick spread as the 0.2 power of time, i.e. very slowly compared to the visible slick

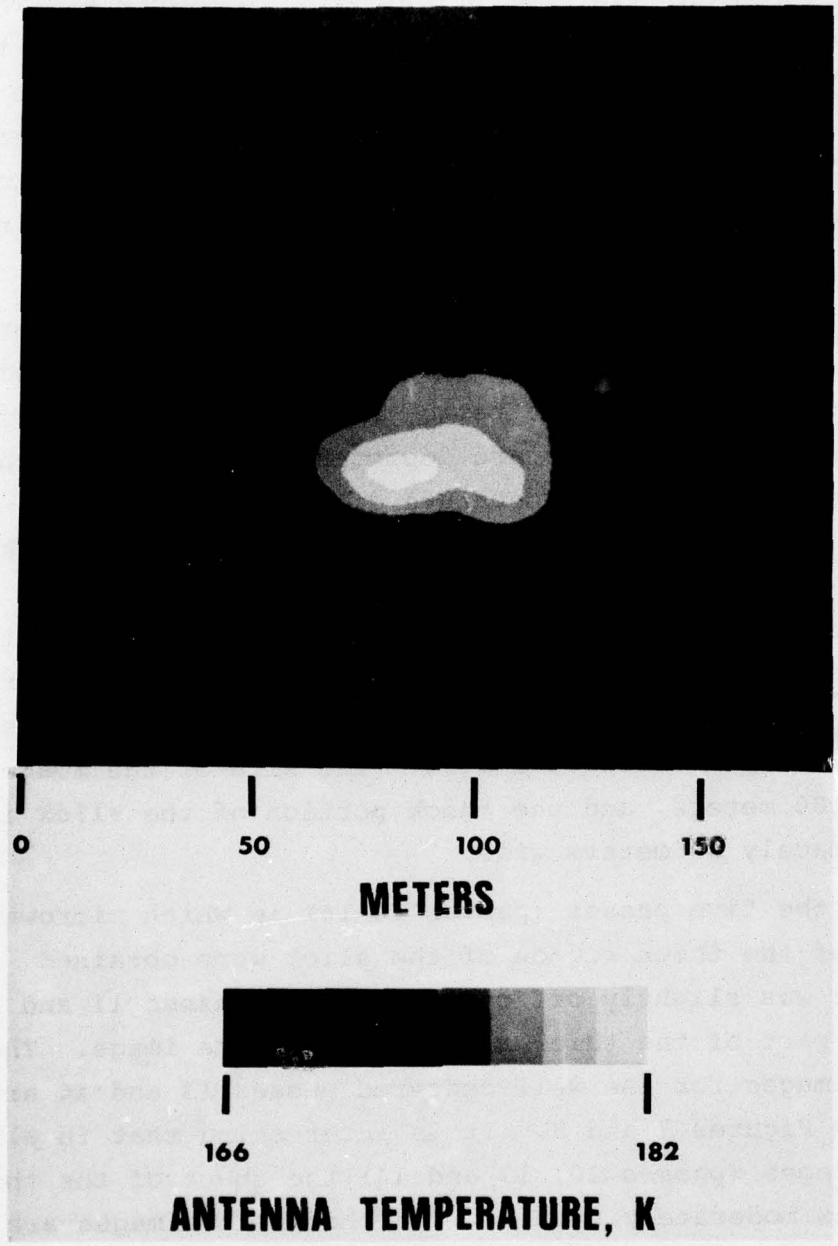

Fig. 6 — 22 GHz antenna temperature contour image of the thick oil region on pass 10. This image is an expansion of the central bright area seen in Fig. 4; the image has been filtered and put in the proper aspect ratio. The lighter area in the upper left corner is open ocean; the dark region is the thin oil area.

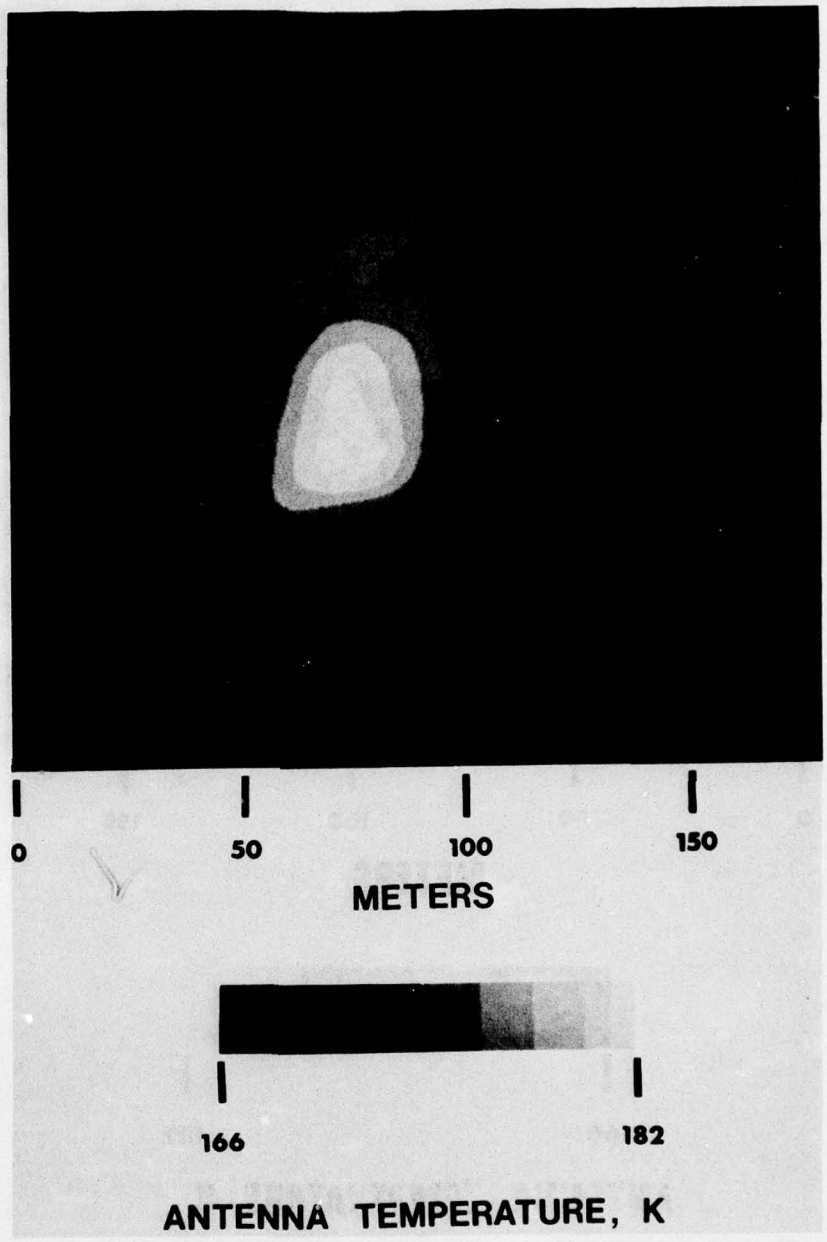

Fig. 7 — 22 GHz antenna temperature contour image of the thick oil region on pass 13

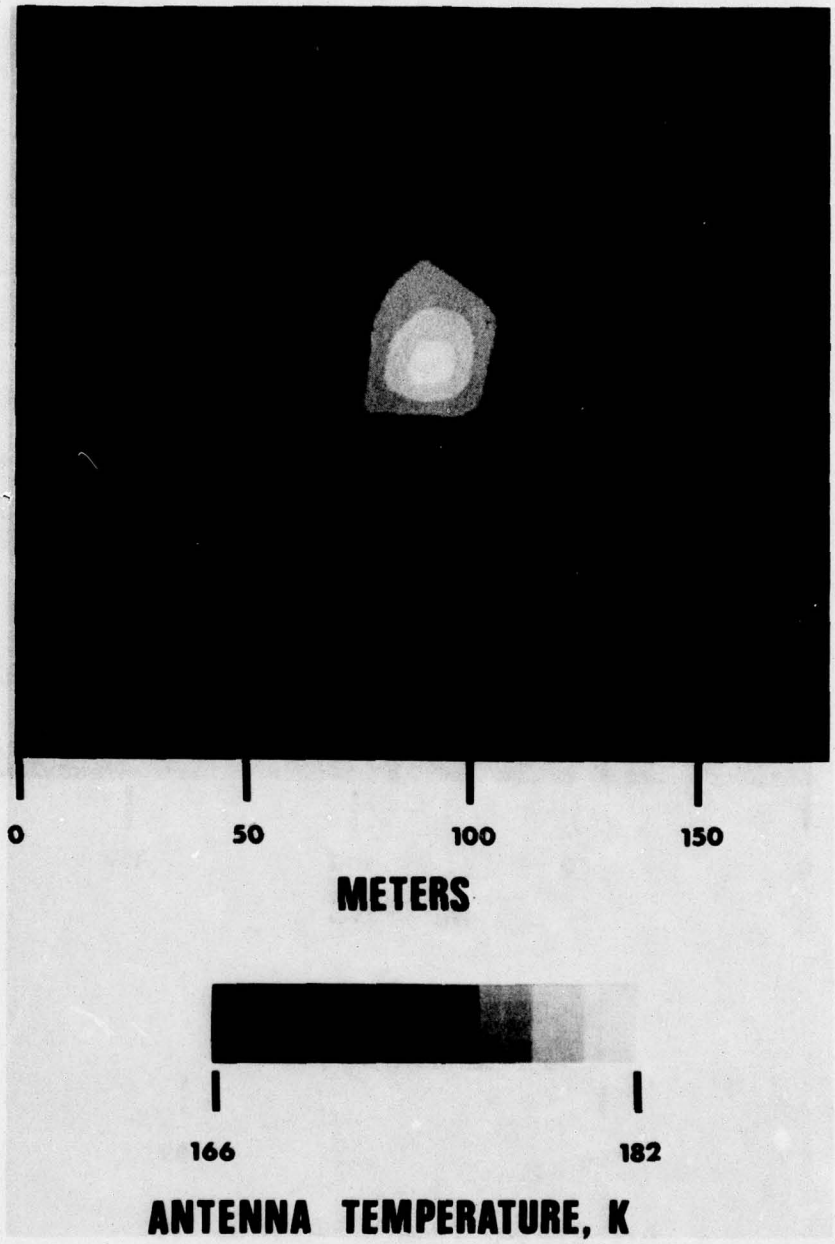

Fig. 8 — 22 GHz antenna temperature contour image of the thick oil region on pass 14. Notice the similarity among Figs. 6, 7, and 8.

which spread as the 0.6 power of time or faster depending upon the wind speed.

Figure 9 shows the 31 GHz antenna temperature image taken in pass 14. Maximum antenna temperature in the oil slick is 159 K, and the average antenna temperature of the sea is 145 K. The 31 GHz image is considerably more complex than the corresponding 22 GHz image given in Figure 8. This complexity is due to a faulty IF amplifier in the 31 GHz radiometer, which made the 31 GHz data very noisy: the RMS deviation of the 22 GHz antenna temperature, is 2.3 K, whereas that of the 31 GHz temperature is 5.7 K, or 2.5 times greater. The result of this malfunction is to lower the quality of the 31 GHz data and make them less reliable for oil volume measurement, as will be seen later in this report.

The next step in the data analysis routine is to determine the increase in brightness temperature of the oil slick over that of the open ocean. For this calculation, the average antenna temperature of the ocean around the slick is computed and subtracted from each temperature value of the array, and the resulting antenna temperature differences ΔT_a are converted to brightness temperature differences ΔT_b by correcting for sky reflection and antenna beam efficiency.

The average ocean antenna temperature $\bar{T}_a$ is derived in the computer program by averaging T_a over a large area of ocean. This value is then subtracted from every value in the filtered array to get an array of temperature differences ΔT_a. Every negative ΔT_a is then set equal to zero. The remaining ΔT_a values are converted to brightness temperature differences (2) by correcting for both antenna beam efficiency and for reflected sky radiation using the equation:

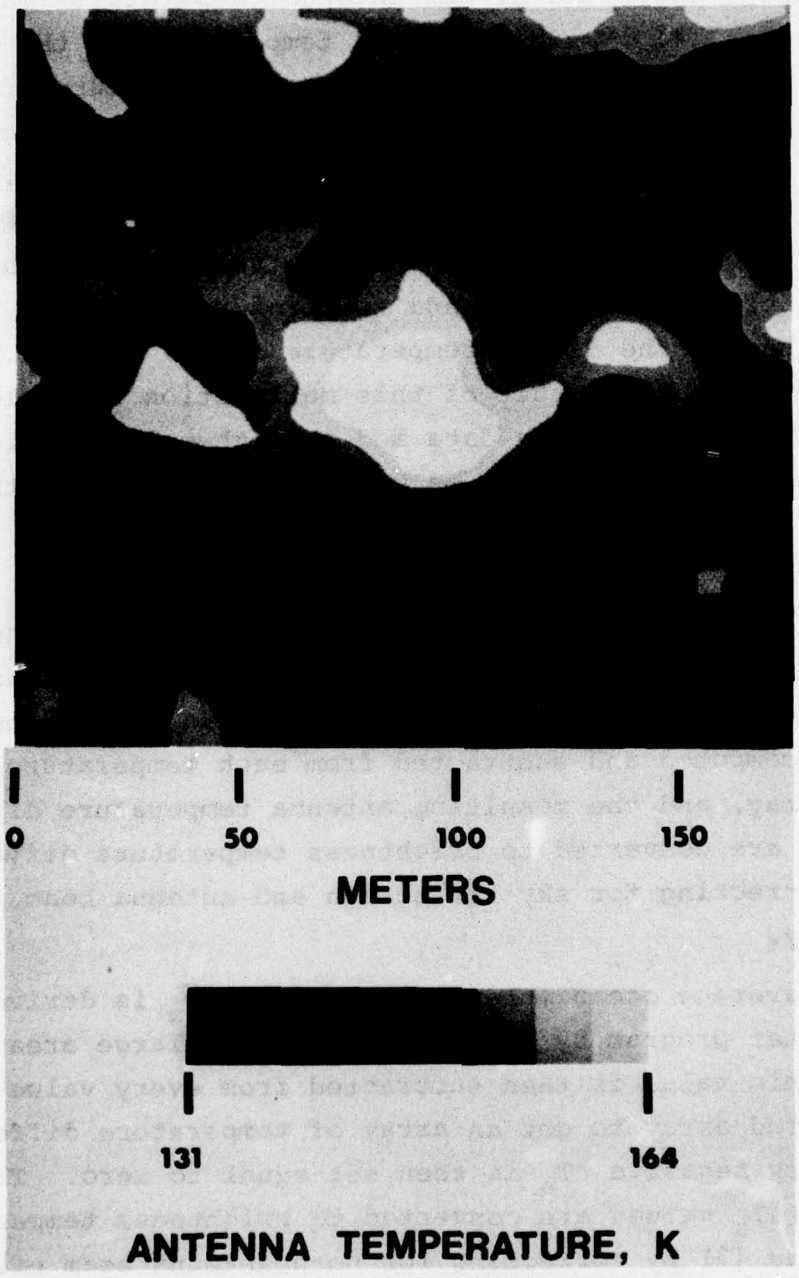

Fig. 9 — 31 GHz antenna temperature contour image of the thick oil region on pass 14. Compare to the corresponding 22 GHz image in Fig. 8.

$$\Delta T_b = \Delta T_a \left[\frac{1}{\eta \left(1 - \frac{T_{sky}}{T_o} \right)} \right] ,$$

where

η = antenna beam efficiency

T_o = physical water temperature

T_{sky} = brightness temperature of the sky.

Ideally, T_{sky} should be measured for both 22 GHz and 31 GHz during the flight, but the radiometer could not be pointed upward to obtain the sky temperature while it was being used for the imager. Therefore, T_{sky} was calculated using a standard atmospheric model and measured environmental factors (temperature, humidity, pressure, cloud type). (The details of the calculations are given in the Appendix of this report.) Most of these environmental measurements were made by the U. S. Coast Guard. For an operational system, T_{sky} could be measured directly by an upward-pointing radiometer, or calculated from measurements or estimates of environmental parameters.

As shown in Figure 5, there is a wind-induced difference of 1-2 K between T_a for the open ocean and T_a for the thin oil slick. It would be preferable in computing ΔT_a to use a reference value $\bar{T}_a$ based on the thin oil slick immediately around the thick oil region, rather than $\bar{T}_a$ based on the open ocean. But to determine $\bar{T}_a$ (thin oil slick) automatically by computer would require considerably greater complexity in the computer program. It can be shown that using $\bar{T}_a$ (open ocean) rather than $\bar{T}_a$ (thin oil slick) introduces an error of less than 10% in the final oil volume computation. This error is less than the overall 25% accuracy claimed for oil volume determination in the earlier test program (2).

After the brightness temperature differences are obtained, they are converted to oil film thickness values. The conversion is accomplished by means of a computer program which computes the brightness temperature of a layer of oil between sea water and air, as a function of the oil thickness. Input information includes the dielectric properties of the oil, sea salinity and ambient temperature. For a detailed description of the calculations, see the Appendix. Figure 10 shows the calculations for the conditions prevailing during the 25 September flights. The brightness temperature difference ΔT_b between T_b (oil film on sea) and T_b (sea water) is plotted at the top of Figure 10 versus the oil film thickness t, for both 22 GHz and 31 GHz. Physically, the oil film acts as a matching layer between air and sea water. As the thickness of the oil film increases, the brightness temperature at first increases and then passes through alternating maxima and minima at successive oil film thicknesses, which are integral multiples of a quarter of the observational wavelength in the oil. The maximum ΔT_b as seen in Figure 10 is approximately 80 K. It is this enhancement of the oil film brightness temperature which allows the location and thickness determination of oil spills by passive microwave techniques. The microwave image, now in the form of a 29 x 29 array of ΔT_b values, is converted to a 29 x 29 array of oil thickness values, element by element, by use of the quantitative ΔT_b vs. thickness information shown in Figure 10.

For a given frequency, there is a one-to-one relation between ΔT_b and t only up to the first maximum in ΔT_b and its corresponding thickness t_m. Consequently, there can be an ambiguity in the thickness measurement when thicknesses greater than t_m are present. For example, if ΔT_b = 50 K for 31 GHz, Figure 10 shows that the oil film thickness can be 0.9 mm, 2.3 mm, or even higher. The ambiguity can be resolved by using simultaneous data at another frequency: at

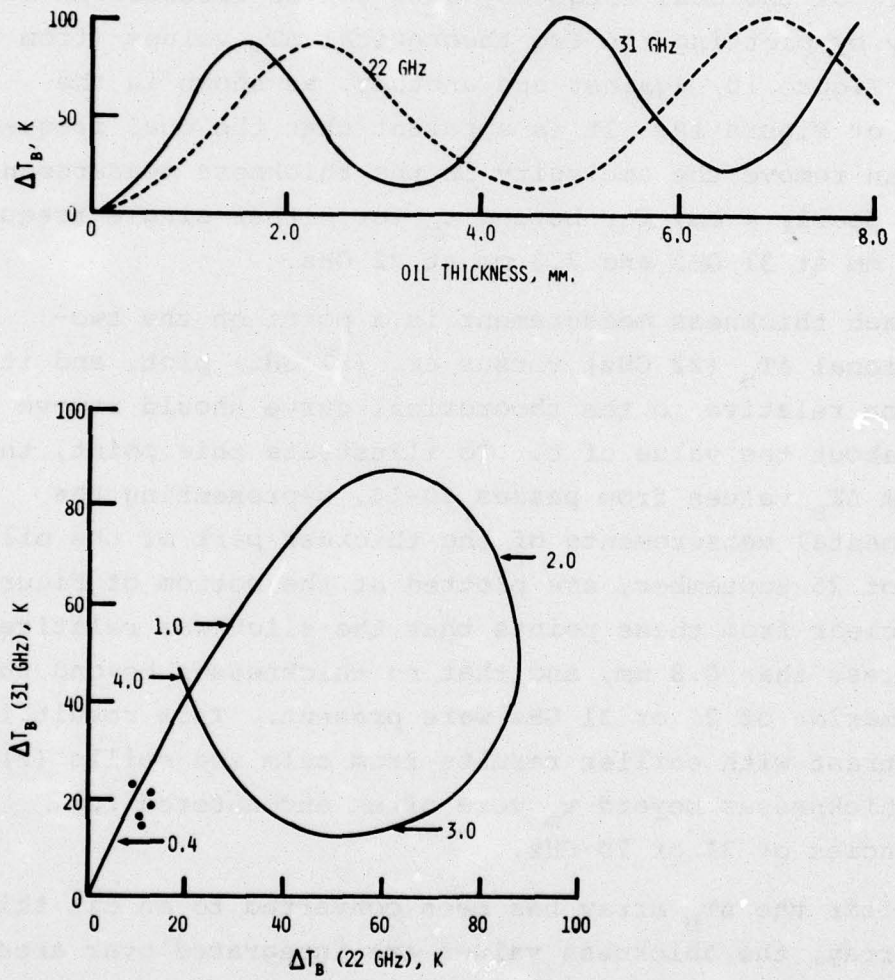

Fig. 10 — Upper graph: the difference in microwave brightness temperature ΔT_b between oil-covered sea and open sea as a function of the oil thickness, for both 22 GHz and 31 GHz. Lower graph: a single plot showing ΔT_b (22 GHz) versus ΔT_b (31 GHz). The arrows represent specific oil thickness values in millimeters. The five data points correspond to the greatest oil thickness values on each of the five passes 10-14.

22 GHz, ΔT_b = 25 K for t = 0.9 mm, and ΔT_b = 87 K for t = 2.3 mm. Therefore, the thickness t = 0.9 mm corresponds to the ordered pair (25, 50), and t = 2.3 mm corresponds to the different ordered pair (87, 50), where the first value is ΔT_b (22 GHz) and the second is ΔT_b (31 GHz). This characteristic of the dual frequency data can be illustrated more readily by plotting the two theoretical ΔT_b values (from the top of Figure 10) against one another, as shown in the bottom of Figure 10. It is apparent that the dual frequency data can remove the ambiguity in the thickness measurement out to nearly 4 mm, far beyond t_m for either single frequency of 1.6 mm at 31 GHz and 2.3 mm at 22 GHz.

Each thickness measurement is a point on the two-dimensional ΔT_b (22 GHz) versus ΔT_b (31 GHz) plot, and its position relative to the theoretical curve should remove any doubt about the value of t. To illustrate this point, the maximum ΔT_b values from passes 10-14, representing the experimental measurements of the thickest part of the oil spill of 25 September, are plotted at the bottom of Figure 10. It is clear from these points that the slick was relatively thin, less than 0.8 mm, and that no thicknesses beyond the first maxima of 22 or 31 GHz were present. This result is in contrast with earlier results from calm sea spills (2) when thicknesses beyond t_m were often encountered for frequencies of 31 or 70 GHz.

After the ΔT_b array has been converted to an oil thickness array, the thickness values are integrated over area to determine the volume in the oil slick. The integration should be confined to the thick region of the slick, since integration of statistical noise in the surrounding area of negligible thickness can make a significant but erroneous contribution to the computed oil volume, especially when the surrounding area is large compared to the thick oil region. To avoid this undesired result, a scheme is adopted which

effectively sets t = 0 for all areas except the thick portion of the slick. First, t is made zero for all points in the 29 x 29 array for which $\Delta T_b < 0$, since negative incremental brightness temperatures are not physically possible for a significant oil film thickness and hence must be spurious. Next, the average thickness t_a is compiled for each 5 x 5 square of points in the array, and when $t_a < 0.1$ mm, t is made zero for the central point in the 5 x 5 array. Figure 11 shows the resulting thickness array for the 22 GHz, pass 13 data as a thickness contour image. The dark spot in the middle represents the oil slick, each grey level corresponding to an oil thickness increment of 0.1 mm. Maximum thickness in the center is approximately 0.6 mm. Statistical noise in the area immediately around the thick region has been effectively suppressed, as evidenced by the large region of white, i.e. zero thickness.

Integration of the thickness values for the entire image yields a volume of 1359 liters. If the integration is restricted to the large contiguous dark region near the center, thereby eliminating the small remaining noise from the integration, the resulting volume is 1223 liters. This value is the most accurate estimate of the oil volume in the image, and is less than the 2040 liters actually spilled from the CHEROKEE. It is felt that the smaller figure represents the true oil volume in the image, and that the discrepancy is due to the lack of a proper point spill being achieved. This contention is in agreement with the results from the earlier spills (2). When the spill was conducted from small rubber boats, a single cohesive thick region was formed; but when the spill was conducted from the large U. S. Coast Guard ship, the thick region was generally fragmented and spread out, presumably by the motion of the ship. Since the 25 September 1975 spill was made from the USCG CHEROKEE, it is logical to suspect that the thick

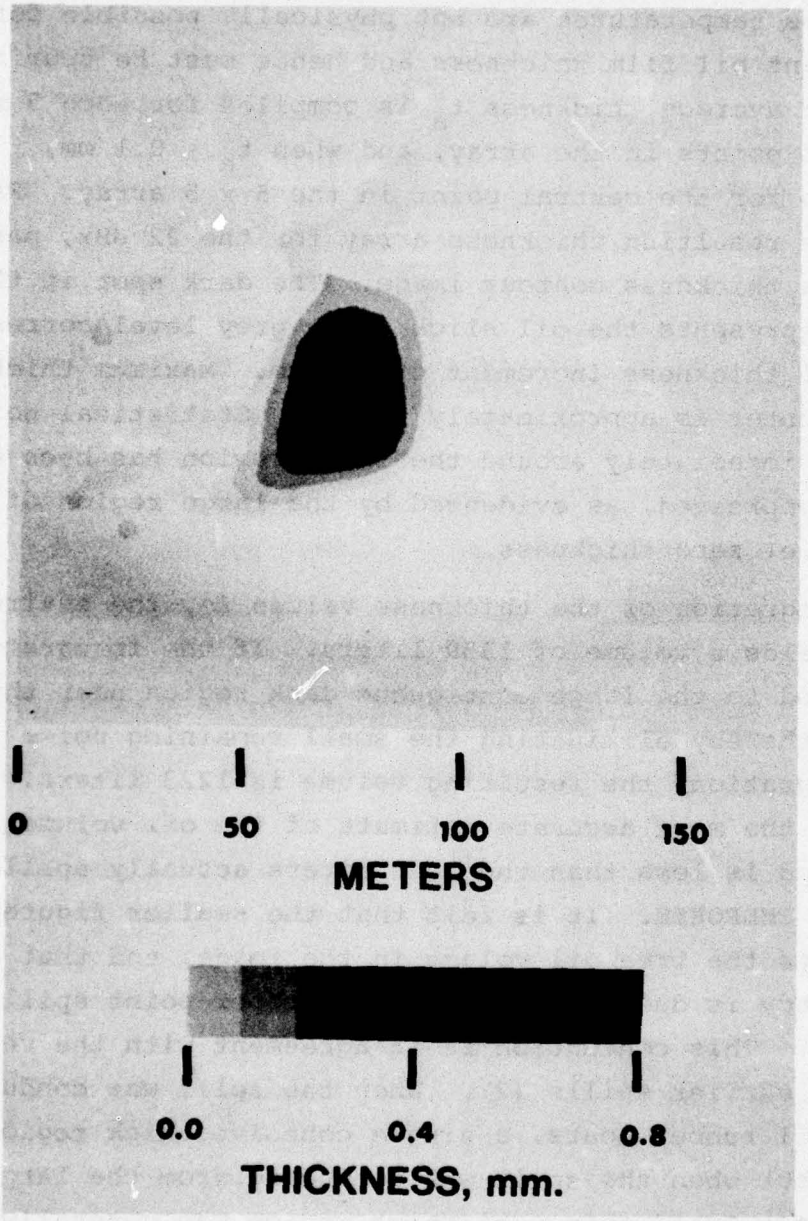

Fig. 11 — Oil thickness contours derived from the 22 GHz antenna temperatures of pass 14

region depicted in Figure 11 is one of several such regions, and that the computed volume of 1223 liters is not in error, but represents the fraction of the total volume actually present in the field of view of the imager.

Figure 12 shows the pass 13 thickness contours derived from the 31 GHz data, corresponding to the 22 GHz data in Figure 11. The oil region is less distinct in the 31 GHz image than in the 22 GHz image, and the 31 GHz image is generally noisier. This result is to be expected because of the previously-mentioned large RMS noise of approximately 6 K in the 31 GHz data. The value of the oil volume obtained from computer integration of the whole image is 1760 liters, and from the main slick is 700 liters.

The 22 GHz thickness contour image for pass 14 is given in Figure 13. Notice that the shape of the thick oil region has not changed greatly, and that an extension of the thick region still persists in the top of the figure. The integrated volume for the whole image is 1408 liters, and form the main slick, 1094 liters. The oil volumes are summarized in Table 2.

On passes 11 and 12, the C-54 did not pass directly over the thick oil region, so that the thick region was partially off the image. The 22 GHz image for pass 11 is shown in Figure 14. The extension of the thick region, which can be seen in Figures 11 and 13, apparently extends off the image in Figure 14. As expected, integration of the isolated thick region yields an oil volume of 852 liters which is less than the corresponding average for the three well-centered passes of 1124 liters.

As described earlier, it is desirable to find a method of automatically reducing the spurious contributions of open ocean and/or noise to the oil volume figure derived by integration of the oil thickness over the entire image. One

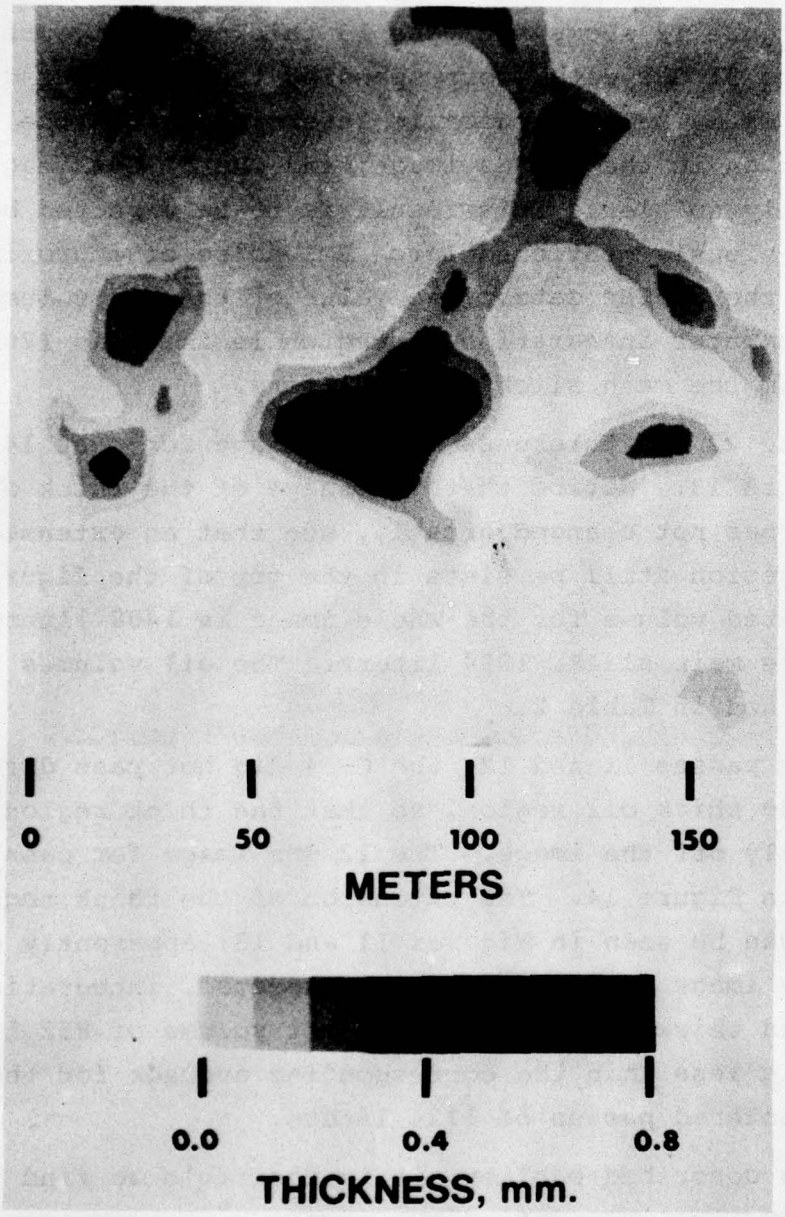

Fig. 12 — Oil thickness contours derived from the 31 GHz antenna temperatures of pass 13. Compare to the corresponding 22 GHz image in Fig. 11.

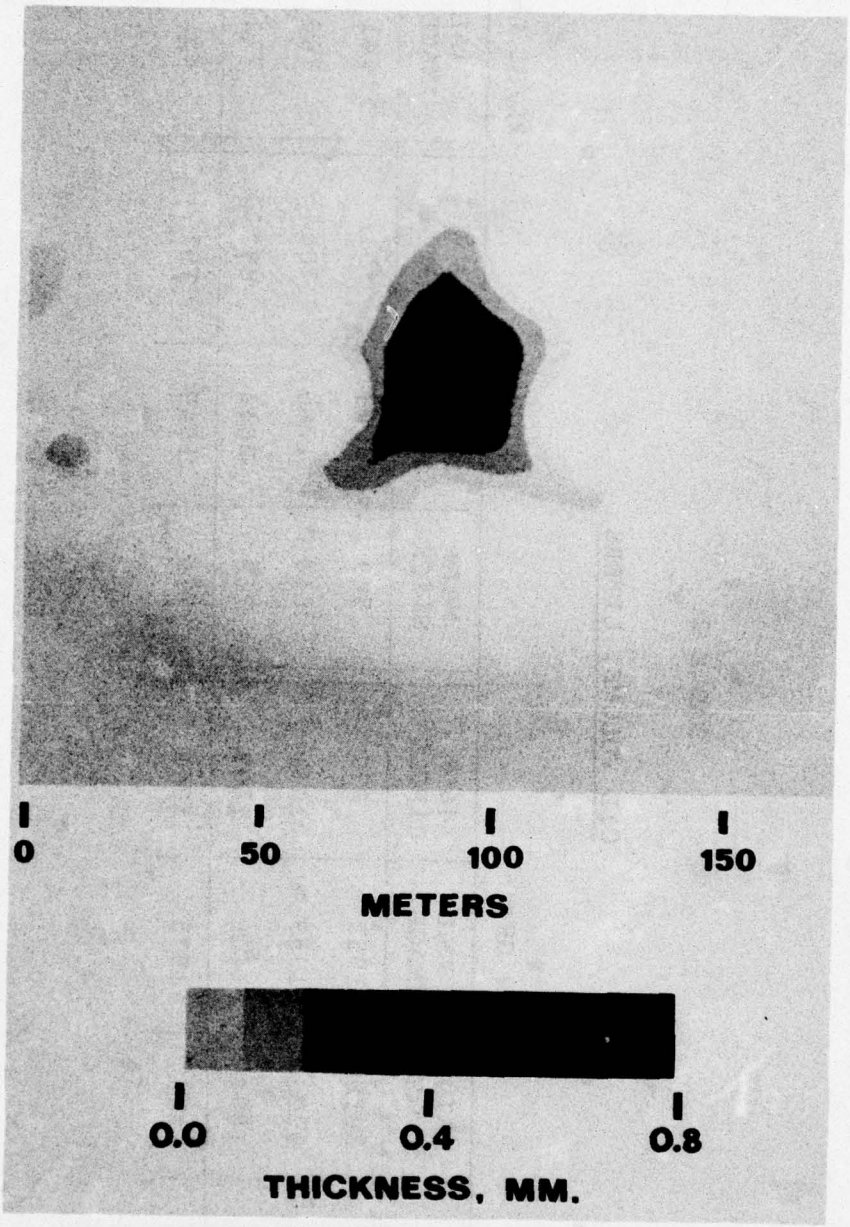

Fig. 13 — Oil thickness contours derived from the 22 GHz antenna temperatures of pass 14

TABLE 2.

OIL VOLUME, LITERS

	22 GHz			31 GHz			22/31 GHZ
	MAIN SLICK	TOTAL IMAGE	46 M CIRCLE	MAIN SLICK	TOTAL IMAGE	46 M CIRCLE	TOTAL IMAGE
PASS 10	1056	1953	977	749	2048	791	1041
PASS 13	1223	1359	1041	640	1760	700	746
PASS 14	1094	1408	1109	768	2044	882	772
AVERAGE	1124	1575	1041	719	1949	791	852

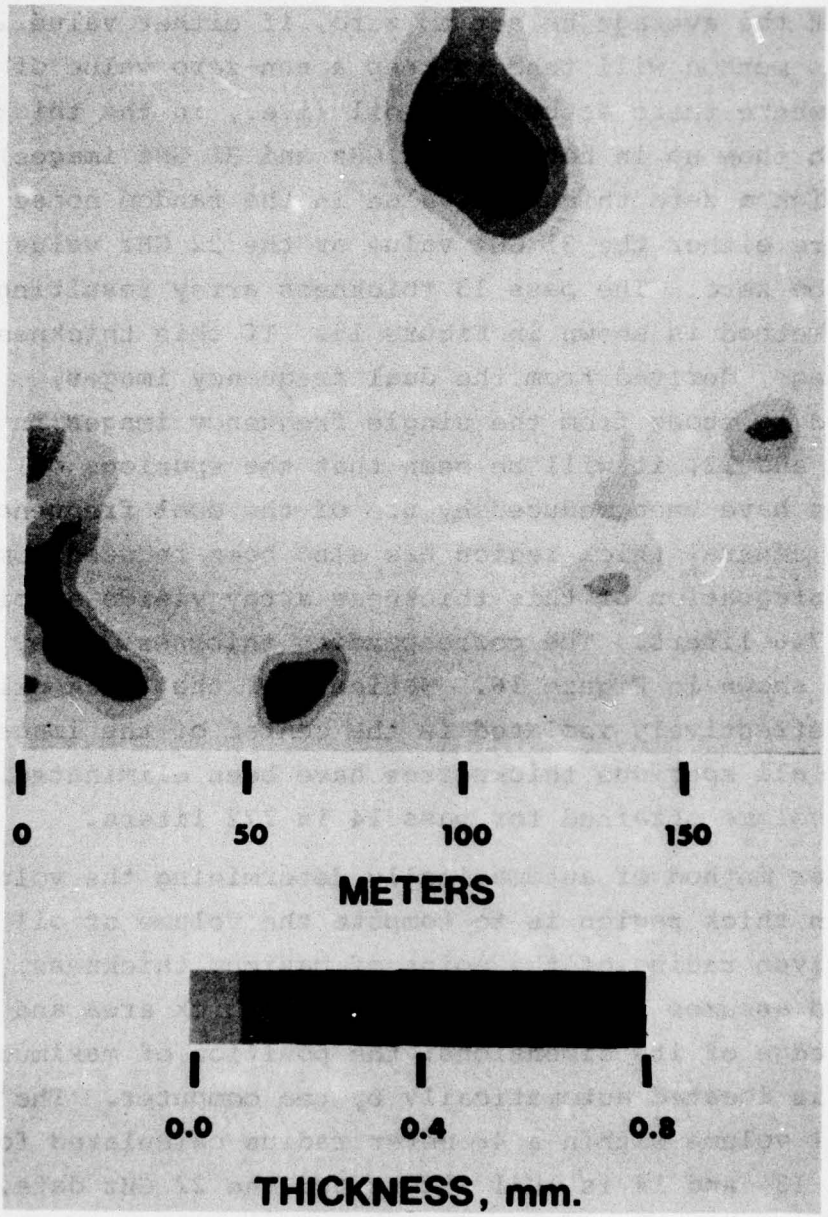

Fig. 14 — Oil thickness contours derived from the 22 GHz antenna temperatures of pass 11. The aircraft did not pass directly over the thick oil on this pass, so that part of the thick oil is off the image.

method of eliminating noise is to generate a new thickness array by averaging the thickness values derived from the 22 GHz and the 31 GHz data, pixel by pixel, with the stipulation that the average be set to zero, if either value is zero. This method will tend to keep a non-zero value of thickness where there actually is oil (i.e., in the thick areas which show up in both the 22 GHz and 31 GHz images), but to assign a zero thickness value in the random noise areas, where either the 31 GHz value or the 22 GHz value is likely to be zero. The pass 13 thickness array resulting from this method is shown in Figure 15. If this thickness contour image, derived from the dual frequency images, is compared to those from the single frequency images in Figures 11 and 12, it will be seen that the spurious oil thicknesses have been reduced by use of the dual frequency data. The central thick region has also been reduced somewhat. Computer integration of this thickness array yields an oil volume of 746 liters. The corresponding thickness array for pass 14 is shown in Figure 16. Notice that the thick oil region is effectively isolated in the center of the image and almost all spurious thicknesses have been eliminated. The total volume obtained for pass 14 is 772 liters.

Another method of automatically determining the volume in the main thick region is to compute the volume of oil within a given radius of the point of maximum thickness. This method assumes a well-defined single thick area and some knowledge of its dimensions; the position of maximum thickness is located automatically by the computer. The average oil volume within a 46 meter radius calculated for passes 10, 13, and 14 is 1041 liters for the 22 GHz data, and 791 liters for the 31 GHz data. Notice that these values agree reasonable with the corresponding volumes for the main slick. Details are given in Table 2.

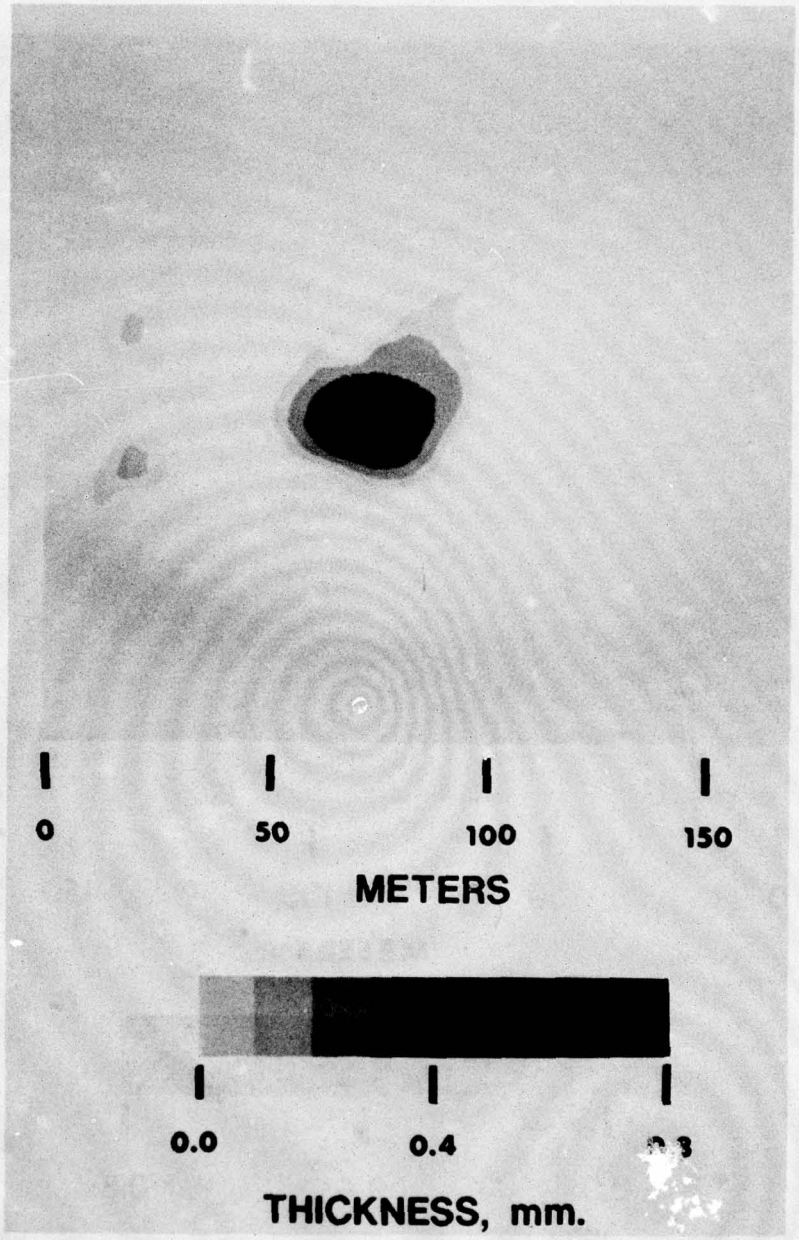

Fig. 15 — Oil thickness contours derived from simultaneous use of both 22 GHz and the 31 GHz antenna temperatures of pass 13. Compare to Figs. 11 and 12, and notice that the noise has been greatly reduced.

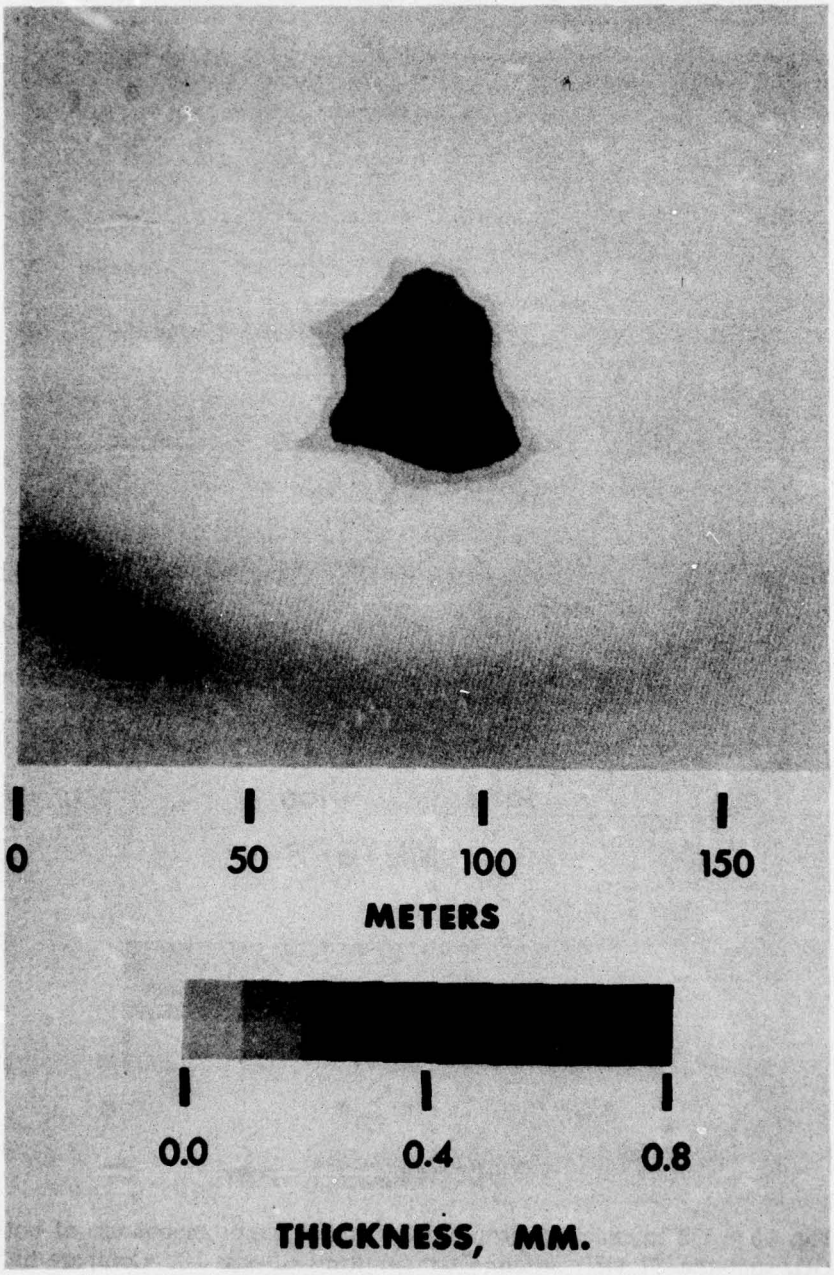

Fig. 16 — Oil thickness contours derived from simultaneous use of both the 22 GHz and 31 GHz antenna temperatures of pass 14. Compare to Fig. 13.

Throughout the data analysis, images made from the 22 GHz data have been considerably cleaner in appearance than those made from the 31 GHz data, with the oil region standing out much more clearly against the background. A comparison between the antenna temperature images at 22 and 31 GHz given in Figures 8 and 9 and between the derived oil thickness contours given in Figures 11 and 12 will illustrate this difference. The greater complexity of the 31 GHz images stems from the noisier 31 GHz data; the RMS antenna temperature deviation of 6 K is great enough to strongly affect the images, when the maximum antenna temperature increase due to the oil is less than 20 K. It is reasonable to assume that for this flight, the results from the 22 GHz data will be more meaningful than the corresponding results from the 31 GHz data, and that attempts to eliminate noise by combining the data from the two frequencies will suffer because of the noisy 31 GHz data. It should be noted that in the previous program the 31 GHz radiometer consistently provided the smoothest data (see Figures 44 and 52 of reference 2). Had it performed as well in this flight as it performed previously, the 31 GHz data would have been fully as good as the 22 GHz data. The decreased performance of the 31 GHz radiometer in this flight was due only to a malfunctioning component, and should not prejudice its use in any future program.

SUMMARY

The NRL microwave imager has been used to detect an oil slick on the surface of the ocean, and to make microwave brightness temperature images of the slick. In these images, the slick shows up clearly against the ocean background. It is seen that the oil tends to concentrate in small thick regions, with a maximum thickness on the order of 1 mm, on the down-wind side of a much larger and thinner slick, in

agreement with results from previous flights (2). The use of microwave imagery on this flight represents a great advance over the use of fixed radiometers in the earlier flights, because a complete picture of the oil spill can be made with the imager in one aircraft pass of a few seconds duration, whereas the earlier flights required approximately a dozen passes, taking nearly an hour, to acquire the same information. Consequently, the imager represents a large step towards a quick-response, real-time oil spill detection system.

Computer software has been developed which converts the temperature images to thickness images, and integrates the thickness to obtain oil volume. The dual frequency capability of the imager is used to avoid ambiguity in the oil thickness measurement, and to eliminate noise in the ocean background which makes a spurious contribution to the determination of oil volume. Contour images of the oil slick thickness are produced so that the shape, area and thickness of the slick can be readily visualized. Oil volume of the thick region is automatically computed by two methods and the results are printed out. This data processing method, making use of the imager's ability to obtain a microwave snapshot of the oil slick, is a considerable improvement over the processing of data taken in the earlier fixed-radiometer flights. Basically, data taken in the earlier flights required time consuming post flight analysis, whereas imager data are automatically processed by computer in a manner which would allow real-time analysis during actual overflights of the slick.

ACKNOWLEDGMENTS

The authors are indebted to LTCDR A. Maurer of the U.S. Coast Guard, who conducted the oil spills and was contract monitor. We also wish to thank the air crews and personnel at NASA-Wallops Flight Center for providing the aircraft support.

REFERENCES

1. Hollinger, J. P. and Mennella R. A., "Oil Spills: Measurements of Their Distributions and Volumes by Multifrequency Microwave Radiometry," Science, Vol. 181, pages 54-56, July 6, 1973.

2. Hollinger, J. P., "The Determination of Oil Slick Thickness by Means of Multifrequency Passive Microwave Radiometry," Final Report prepared for the U. S. Coast Guard, NRL Memorandum Report 2953, U. S. Coast Guard Report CG-D-31-75, June 30, 1974.

3. Hollinger J. P., Kenney, J. E., and Troy B. E., "A Versatile Millimeter-Wave Imaging System," IEEE Transactions on Microwave Theory and Techniques, MTT-24, pages 786-793, November, 1976.

4. Jurkevich, I., Lee, J., and Petty, A. F., A description of the system is in preparation, 1976.

5. Harmon, L. D. and Julesz, B., "Masking in Visual Recognition: Effects of Two-Dimensional Filtered Noise," Science, Vol. 180, pages 1194-1197, June 15, 1973.

APPENDIX A

The microwave radiation received from the ocean surface is composed of the radiation emitted by the surface, the radiation emitted by the atmosphere between the observer and the surface and the downwelling atmospheric and cosmic background radiation reflected or scattered from the surface to the observer. Further, the radiation emitted and reflected from the surface is attenuated by the atmosphere between the surface and the observer. The polarization state of both emitted and reflected radiation may be specified by the intensities in any two orthogronal directions[1]. However it is customary to select "horizontal" (h) and "vertical" (v) defined as being when the electric field vector is perpendicular or parallel to the plane of incidence on the surface.

The intensity of the radiation in watts/M^2/Hz/steradian with the vertical polarization emitted by a non-uniform surface in a direction (θ_o,ϕ_o) is shown by Peake (1) to be

$$I_{ev}(o) = \left\{1-\frac{1}{4\pi}\int[\gamma_{vv}(o,s) + \gamma_{vh}(o,s)]\, d\Omega_s\right\} I_{bv}. \quad \text{(A-1)}$$

Here the letter (o) is an abbreviation for the angles (θ_o,ϕ_o) and the letter (s) for the angles (θ_s,ϕ_s). The

---

[1]We consider here only "natural" radiation where no permanent phase relationship exists between orthogonal states. In the case of coherent radiation, the phase between the two orthogonal components must also be given to completely specify the polarization state.

integration is over the upper hemisphere. The γ's are the surface scattering coefficients defined by Peake (1) and I_{bv} is the intensity emitted with vertical polarization by a blackbody at the same physical temperature as the surface[2].

$$I_{bv} = (h\nu/\lambda^2)/(\exp(h\nu/KT) - 1) , \qquad (A-2)$$

where h and K are Planck's and Boltzmann's constants respectively, ν the frequency and λ the wavelength of the radiation and T the temperature of the surface. The horizontal component of the radiation is obtained from equation (A-1) by interchanging the subscripts v and h.

The intensity of the downwelling sky radiation reflected from the surface into the direction (θ_o, ϕ_o) with vertical polarization is given by Peake (1) to be

$$I_{rv}(o) = \frac{1}{4\pi} \int [I_{sky\ v}(s)\ \gamma_{vv}(o,s) + I_{sky\ h}(s)\gamma_{vh}(o,s)]d\Omega_s , \qquad (A-3)$$

where $I_{sky\ v}(s)$ and $I_{sky\ h}(s)$ are the intensities of the vertically and horizontally polarized components of the radiation incident on the surface from the direction (θ_s, ϕ_s) and again the integration is to be carried out over the upper hemisphere. The horizontal component of the radiation is obtained, as before, by interchanging the subscripts v and h.

---

[2]Since the radiation originates in the medium beneath the surface and is not actually emitted by the surface, it is assumed that the medium has a well-defined temperature to a depth from which all energy would be absorbed before reaching the surface.

The atmospheric radiation, I_{sky}, for a non-scattering, horizontally stratified atmosphere in local thermodynamic equilibrium is obtained by solving the radiative transfer equation, e.g. (2),

$$\frac{dI_{sky\ v}}{dZ} + \alpha\ I_{sky\ v} = \alpha\ I_{bv}\ . \qquad \text{(A-4)}$$

Here I_{bv} is given by equation (A-2) using the local physical temperature of the atmosphere, α is the absorption coefficient of the atmosphere and dZ, which takes into account the earth's curvature, is given by

$$dZ = \left[1 - \left(\frac{a\ \sin\theta_s}{a + h}\right)^2\right]^{-1/2} dh\ , \qquad \text{(A-5)}$$

where a is the earth's radius, h is the height above the surface and θ_s is the angle between the direction of propagation z and the vertical direction.

The solution of equation (A-4) is greatly simplified when the Rayleigh-Jeans approximation to the Planck blackbody function is appropriate since then the intensity and physical temperature of the radiating body are linearly related. Equation (A-2) then becomes

$$I_{bv} = KT/\lambda^2\ . \qquad \text{(A-6)}$$

This linear relationship also makes it convenient to describe the radiation, not only from black bodies, but from any source in terms of an equivalent blackbody temperature or brightness temperature. The brightness temperature, T_B, is defined as the temperature to which a black body must be raised in order that the black body radiates the same intensity, at frequency ν, as does the source. Then,

$$T_{Bv} = \lambda^2 I_v / K \quad . \qquad \text{(A-7)}$$

The Rayleigh-Jeans approximation to Planck's law is better than one percent for frequencies less than 100 GHz and temperatures greater than 250 K. Certainly at centimeter wavelengths, the approximation is very good but at millimeter wavelength the error becomes progressively larger and is not negligible. However Stogryn (3) has shown that, for the near-earth environment, the error introduced by using the Rayleigh-Jeans approximation can be reduced by at least two orders of magnitude simply by changing the boundary condition describing the downward flowing flux at the top of the earth's atmosphere. This improvement in accuracy results in a negligible error, for earth environmental observations, when the Rayleigh-Jeans approximation is used even at short millimeter wavelengths.

Following Stogryn (3) the solution of equation (A-4) for the downwelling radiation at some height h in the atmosphere is

$$T_{B\ sky\ v} = \int_h^\infty \alpha(h')\ T_{atm}(h')\ L(h,h')dZ' + L(h,\infty)\ T_\infty \ , \qquad \text{(A-8)}$$

where T_{atm} is the local thermodynamic temperature of the atmosphere, L is the transmission factor

$$L(a,b) = \exp\left\{-\int_a^b \alpha\ dZ\right\} \ , \qquad \text{(A-9)}$$

and T_∞ represents the radiation incident upon the top of the atmosphere. In the absence of specific extraterrestrial sources of radiation in the direction (θ_s,ϕ_s), such as the sun, galactic, or extragalactic radio sources, T_∞ is composed only of the cosmic background radiation at a

radiation temperature, T_c, of 2.8 K (4). Stogryn has shown (3) that if T_∞ is taken as

$$T_\infty = (h\nu/K)/(\exp(h\nu/KT_c) - 1) + (h\nu/2K) \qquad \text{(A-10)}$$

rather than simply as T_c, as is customarily done, negligible error results from using the Rayleigh-Jeans approximation.

The vertically polarized component of the total upwelling radiation from the surface and atmosphere at a height h above the surface is, using equations (A-1), (A-3), (A-5), (A-6), and (A-9),

$$T_{Bv} = L(o,h) \left\{ \left[1 - \frac{1}{4\pi} \int (\gamma_{vv} + \gamma_{vh})\, d\,\Omega_s \right] T_{sea} + \frac{1}{4\pi} \int (\gamma_{vv} + \gamma_{vh})\, T_{B\ sky}\, d\,\Omega_s \right\} + \int_o^h \alpha(h')\, T_{atm}(h')\, L(h',h)\, dZ' \,. \qquad \text{(A-11)}$$

Here T_{sea} is the thermodynamic temperature of the sea and $T_{B\ sky}$ is given by equation (A-8) with h = 0. Since the downwelling sky radiation incident on the surface is unpolarized $T_{B\ sky\ v} = T_{B\ sky\ h}$. The horizontally polarized component is obtained by interchanging the v and h subscripts in equation (A-11).

It is now necessary to calculate the atmospheric absorption coefficient α and the surface scattering coefficient γ. The atmosheric absorption coefficient at centimeter and millimeter wavelengths is primarily dependent on molecular oxygen, water vapor and liquid water in the form of fog, clouds, and rain.

The calculation of microwave oxygen absorption is based on the computational scheme suggested by Rosenkranz (5) which relies principally on the work of Gordon (6) and Van Vleck (7). The model takes into account 40 molecular magnetic dipole transitions which couple the total angular momentum states of the molecules to the incident radiation. The angular momentum quantum number N interacts with electron spin to form two more states with total angular momentum number $J = N + 1$ and $J = N - 1$. Transitions between the states $J = N$ and $J = N \pm 1$ permit resonant absorption at frequencies $\nu_N^{\pm}$. These frequencies are grouped between 50 and 60 GHz with one at 119 GHz. Pressure line broadening and temperature dependence are also accounted for. The basic formula relating the absorption coefficient α in nepers per kilometer to frequency ν in gigahertz, pressure P in millibars, and temperature T in Kelvin is:

$$\alpha_{02} = CP^2 \frac{\nu^2}{T^2} \sum_N \phi_N \left[f_N^{+}(\nu) + f_N^{+}(-\nu) + f_N^{-}(\nu) + f_N^{-}(-\nu) + \frac{0.70\, W_b}{\nu^2 + (Pw_b)^2} \right] \qquad \text{(A-12)}$$

The summation is over the odd rotational states from 1 to 39 and

C = 0.330, a constant, for α_{02} in nepers/km,

$\phi_N = \frac{2N+1}{0.725T} \exp\left\{-2.0685 \frac{N(N+1)}{T}\right\}$ is the fractional population of state N,

$$f_N^{\pm}(\nu) = \frac{w_N (d_N^{\pm})^2 + (\nu - \nu_N^{\pm})\, y_N^{\pm}}{(\nu - \nu_N^{\pm})^2 + (P w_N)^2}$$ are shape factors for the transition lines,

$$d_N^{+} = \left[\frac{N(2N+3)}{(N+1)(2N+1)}\right]^{1/2}$$ and

$$d_N^{-} = \left[\frac{(N+1)(2N-1)}{N(2N+1)}\right]^{1/2}$$ are the amplitudes of the positive and negative transition lines at ν_N^{+} and ν_N^{-},

$w_b = 0.48 \times 10^{-3}\left(\frac{300}{T}\right)^{0.89}$ GHz/mbar is the non-resonant line width used, and

$$y_N^{\pm} = d_N^{\pm}\left\{\frac{2 d_{N+2}^{\pm}\, w_{N\ UP}}{\nu_N^{\pm} - \nu_{N+2}^{\pm}} + \frac{2 d_{N-2}^{\pm}\, w_{N\ DN}}{\nu_N^{\pm} - \nu_{N-2}^{\pm}} - \frac{w_b}{\nu_N^{\pm}} - \frac{w_b}{\nu_N^{\pm} + 60}\right\}$$ are the interference coefficients for coupling between near states due to molecular collisions.

The resonant half widths w_N are computed as

$$w_N = 1.16 \times 10^{-3}\left(\frac{300}{T}\right)^{0.85} ,$$

and the line widths for the collisional coupling are computed in a sequence using the formulas

$$w_{NDN} = w_b - w_N - w_{NUP} , \text{ and}$$

$$w_{N-2\ UP} = w_{NDN}\,\frac{\phi_N}{\phi_{N-2}} .$$

This analysis does not take into account high altitude Zeeman splitting (about 40 km) nor the doppler broadening above 80 km. However, since comparatively little absorption takes place due to low pressure at high altitudes, Zeeman and doppler may be neglected in almost all remote sensing applications except possibly high altitude upward looking radiometers for which a more involved computation is necessary.

The microwave absorption due to water vapor is based on Staelin's (8) intepretation of Barrett and Chung's (9) formula which in turn uses experimental results of several authors to extend Van Vlecks's (10) work on the subject. There is one principal rotational transition for water vapor which significantly affects microwaves and it has a frequency of 22.235 GHz. The equation used to calculate α in nepers per kilometer is:

$$\alpha_{H_2O} = \left[3.24 \times 10^{-4} \exp\left(-\frac{644}{T}\right) \frac{\nu^2 P \rho}{T^{3.125}} \left(1 + 0.0147 \frac{\rho T}{P}\right) \times \left(\frac{1}{(\nu-\nu_o)^2 + \Delta\nu^2} \quad \frac{1}{(\nu+\nu_o)^2 + \Delta\nu^2} \right) + 2.55 \times 10^{-8} \frac{\rho \nu^2 \Delta\nu}{T^{1.5}} \times 10^5 \right], \qquad \text{(A-13)}$$

where

ρ = water vapor density in gm/m^3,

ν_o = 22.235 GHz,

P = total pressure in millibars, and

$$\Delta\nu = 2.58 \times 10^{-3} (P + 0.0147 \rho T) \left(\frac{T}{318}\right)^{-0.625} .$$

The absorption coefficient, in nepers per kilometer, due to liquid water is based on Paris's Thesis (11) and is given by

$$\alpha_L = 0.0629 \left[\frac{3E_2}{(2 + E_1)^2 + E_2^2} \right] \rho_L \nu \quad , \tag{A-14}$$

where E_1 and E_2 are the real and imaginary parts respectively of the relative dielectric constant of water, and

ρ_L is the density of liquid water in gm/m^3.

The dielectric properties of water are not only necessary for the determination of the absorption coefficient due to liquid water but are also required in calculating the emission and reflection properties of the sea surface. The complex dielectric constant of water E may be written as,

$$E = E_o \, (E_1 - jE_2) \quad , \tag{A-15}$$

where E_o is the dielectric constant of a vacuum. The real and imaginary parts of the relative dielectric constant of water are well represented by,

$$E_1 = \frac{(E_s - E_\infty)}{1 + (2\pi\nu\tau)^2} + E_\infty \tag{A-16}$$

$$E_2 = \frac{(E_s - E_\infty)(2\pi\nu\tau)}{1 + (2\pi\nu\tau)^2} + \frac{2\sigma}{\nu} \quad . \tag{A-17}$$

Here ν is the frequency in Hz, τ is the relaxation time in seconds, σ is the ionic conductivity in ESU[3], E_s is the

[3] 1 ESU = $4\pi E_o$ MHOS/meter in MKS units.

static relative dielectric constant and E_∞ is the relative dielectric constant at very high frequencies. Both E_s and E_∞ are dimensionless.

The static dielectric constant, relaxation time, and conductivity are functions of salinity and temperature. To calculate the dielectric properties of water for any combination of salinity and temperature a second order polynomial in salinity and temperature was fitted by the method of least squares to the experimentally determined values of E_s, τ, and σ given by Saxton and Lane (12).

$$E_s = 88.00 - 4.339\times10^{-1}\,S + 1.710\times10^{-3}\,S^2 - 4.035\times10^{-1}\,T + 8.065\times10^{-4}\,T^2 + 6.170\times10^{-3}\,ST - 8.910\times10^{-5}\,S^2T - 6.934\times10^{5}\,ST^2 + 1.439\times10^{-6}\,S^2T^2 \qquad \text{(A-18)}$$

$$\tau = (18.70 - 7.924\times10^{-2}\,S + 6.350\times10^{-4}\,S^2 - 5.489\times10^{-1}T + 5.758\times10^{-3}\,T^2 + 1.889\times10^{-3}\,ST - 7.209\times10^{-6}\,S^2T - 5.299\times10^{-7}\,ST^2 - 2.101\times10^{-7}\,S^2T^2)\times10^{-12} \qquad \text{(A-19)}$$

$$\sigma = (7.788\times10^{-3}\,S - 1.672\times10^{-6}\,S^2 - 8.570\times10^{-15}\,T + 2.996\times10^{-16}\,T^2 + 4.059\times10^{-4}\,ST - 3.215\times10^{-6}\,S^2T - 1.423\times10^{-6}\,ST^2 + 3.229\times10^{-8}\,S^2T^2)\times10^{11}. \qquad \text{(A-20)}$$

The constant value of 4.9 given by Saxton and Lane (12) is used for E_∞.

The surface scattering coefficients, γ, depend upon the ocean surface roughness which arises from two effects (13), (14), (15), (16). The first effect results from the

increasing roughness of the compact water surface and the second effect from the increasing coverage of white caps and sea foam streaks with increasing wind speed. Both effects increase with wind speed and frequency and depend upon the incidence angle and polarization. The surface roughness effect is closely coupled to the local wind field; rapidly responding to changes in the local wind and hence is relatively insensitive to the energy content of low frequency gravity waves. Evidence indicates (13) that it is primarily dependent upon the mean square surface slope and is thus due to surface waves of dimensions comparable to and shorter than the observational wavelength. The sea foam effect results from the increase in the effective microwave emissivity caused by the distortion of the surface by the foam bubble structure, and its increasing coverage with wind speed. The determination of the wind speed dependence is complicated by the fact that the foam coverage of the sea surface and the roughness effect depend, not only on the local wind, but also on the air-sea temperature difference, the duration and fetch of the wind, as well as on the history of the wave spectrum of the sea area being observed.

Although several models have been developed for the calculation of the scattering coefficients (17), (18), (19), (20) none is completely satisfactory. The choice of the model to be used depends upon the situation and conditions to be described. Under calm sea conditions, the Fresnel coefficients for a specular dielectric interface may be used. If roughness effects are not too severe, it is satisfactory to couple this specular solution with an empirical expression for the increase in emission due to surface roughness. For all of the calculations in this report the roughness effect was assumed to be negligible and the solution for a specular surface was used.

The power reflection coefficient for horizontally polarized radiation incident at an angle θ on a specular sea covered with m - 1 smooth horizontally stratified dielectric layers is, following Wait (21),

$$R_h = \frac{\rho_{12}^2 + 2\rho_{12} Y_2 \cos(\phi_{12} - \psi_2) + Y_2^2}{1 + 2\rho_{12} Y_2 \cos(\phi_{12} + \psi_2) + \rho_{12}^2 Y_2^2} \quad . \qquad \text{(A-21)}$$

The phase change occuring during reflection is

$$\text{Tan } X_h = \frac{(\rho_{12}^2 - 1) Y_2 \sin\psi_2 + (Y_2^2 - 1) \rho_{12} \sin\phi_{12}}{(\rho_{12}^2 + 1) Y_2 \cos\psi_2 + (Y_2^2 + 1) \rho_{12} \cos\phi_{12}} \quad . \qquad \text{(A-22)}$$

Here

$$Y_i = \left[\frac{\rho_{ij}^2 + 2\rho_{ij} Y_j \cos(\phi_{ij} - \psi_j) + Y_j^2}{1 + 2\rho_{ij} Y_j \cos(\phi_{ij} + \psi_j) + \rho_{ij}^2 Y_j^2}\right]^{1/2} e^{-2D_i b_i} \quad , \qquad \text{(A-23)}$$

$$\text{Tan } \psi_i = \left[\frac{\rho_{ij} \sin(\phi_{ij} + 2D_i a_i) + Y_j \sin(\psi_j + 2D_i a_i)}{\rho_{ij} \cos(\phi_{ij} + 2D_i a_i) + Y_j \cos(\psi_j + 2D_i a_i)} \cdots \right.$$

$$\left. \cdots \frac{-\rho_{ij}^2 Y_j \sin(\psi_j - 2D_i a_i) - \rho_{ij} Y_j^2 \sin(\phi_{ij} - 2D_i a_i)}{+\rho_{ij}^2 Y_j \cos(\psi_j - 2D_i a_i) - \rho_{ij} Y_j^2 \cos(\phi_{ij} - 2D_i a_i)}\right] , \qquad \text{(A-24)}$$

$$\rho_{ij} = \left[\frac{(a_i - a_j)^2 + (b_i - b_j)^2}{(a_i + a_j)^2 + (b_i + b_j)^2}\right]^{1/2} , \qquad \text{(A-25)}$$

and

$$\text{Tan}\phi_{ij} = \frac{2(a_j b_i - a_i b_j)}{(a_i^2 + b_i^2) - (a_j^2 + b_j^2)} , \qquad \text{(A-26)}$$

where

$$a_i = \frac{2\pi}{\lambda}\left\{\frac{1}{2}\left[\sqrt{(E_{1i}-E_{11}\sin^2\theta)^2 + (E_{2i}-E_{21}\sin^2\theta)^2} + (E_{1i}-E_{11}\sin^2\theta)\right]\right\}^{1/2} , \qquad \text{(A-27)}$$

and

$$b_i = \frac{2\pi}{\lambda}\left\{\frac{1}{2}\left[\sqrt{(E_{1i}-E_{11}\sin^2\theta)^2 + (E_{2i}-E_{21}\sin^2\theta)} - (E_{1i}-E_{11}\sin^2\theta)\right]\right\}^{1/2} . \qquad \text{(A-28)}$$

The indexing used is that the atmosphere above the surface is i = 1, the first dielectric layer is i = 2, the last layer is i = m, the sea is i = m + 1 with $Y_{m+1} = 0$, $\psi_{m+1} = 0$, and j = i + 1. D_i is the thickness and E_{1i} and E_{2i} the real and imaginary parts of the relative dielectric constant of the i^{th} medium. The wavelength of the radiation is λ.

To obtain the power reflection coefficient for vertically polarized radiation, c_i and d_i should be substituted for a_i and b_i in equations (A-24), (A-25) and (A-26) where,

$$c_i = \left(\frac{\lambda}{2\pi}\right)^2 \frac{(a_i E_{1i} + b_i E_{2i})}{(E_{1i}^2 + E_{2i}^2)} , \qquad \text{(A-29)}$$

and

$$d_i = \left(\frac{\lambda}{2\pi}\right)^2 \frac{(b_i E_{1i} - a_i E_{2i})}{(E_{1i}^2 + E_{2i}^2)} \quad . \tag{A-30}$$

The oil covered sea is represented by m = 2 where i = 1 is the atmosphere, i = 2 the oil film and i = 3 the sea. The dielectric properties of the oil were taken as $E_{12} = 2.1$ and $E_{22} = 0.01$.

For a specular surface, Peake (1) has shown that the scattering coefficients have a delta function representation and equation (A-11) becomes

$$T_{B_v} = L(o,h)\left\{ [1 - R_v]\, T_{sea} + R_v\, T_{B\ sky}\right\} + \int_o^h \alpha\, T_{atm}\, L(h',h)\, dZ' \quad , \tag{A-31}$$

where $T_{B\ sky}$ is given by equation (A-8) and R_v by (A-21).

In order to sum up the various radiations and convolve the sum with the antenna pattern, it is necessary to keep track of the polarization and intensity of the radiations. This is conveniently done by specifying the radiation in terms of Stokes parameters (2), since the Stokes parameters for the sum of several independent radiations is the sum of the Stokes parameters of the separate radiations. The Stokes parameters for the incoherent radiation given by equation (A-31) are

$$I_s = \frac{K}{\lambda^2} (T_{B_v} + T_{B_h}) \quad , \tag{A-32}$$

$$Q_s = \frac{K}{\lambda^2} (T_{B_v} - T_{B_h}) \quad ,$$

$$U_s = 0 \ ,$$

$$V_s = 0 \ .$$

Let the Stokes parameters describing the reception properties of the antenna be represented by $[I_a, Q_a, U_a, V_a]$, then the power received by the antenna per unit frequency interval is (22),

$$P = (A_e/2) \int [I_s I_a + Q_s Q_a + U_s U_a + V_s V_a] \, d\Omega \ , \qquad \text{(A-33)}$$

where A_e is the effective area of the antenna. The effective area may be found from the normalized antenna response pattern $f(\theta,\phi)$ and a measurement of the radiation effeciency η of the antenna or a measurement of the maximum gain of the antenna G_o where

$$A_e = \eta\lambda^2 / \int f(\theta,\phi) \, d\Omega = \lambda^2 \, G_o/4\pi \ . \qquad \text{(A-34)}$$

Measurement of η is generally very difficult in practice and, since it is usually very close to unity, it is often taken to be one.

The power received by the antenna is often specified in terms of the so called antenna temperature T_A. This is the temperature to which an impedance, equal to the impedance of the antenna, would have to be raised in order that when it is substituted for the antenna it deliver the same power to the input of the receiver, as does the antenna. The antenna temperature is related to the power received per unit frequency interval by

$$T_A = P/k \ . \qquad \text{(A-35)}$$

REFERENCES

1. Peake, W. H., "Interaction of Electromagnetic Waves with Some Natural Surfaces," IRE Trans. on Antennas and Propagation (Special Suppl.), Vol. AP-7, pp. S324-S329, December 1959.

2. Chandrasekhar, S., "Radiative Transfer," Dover Publ. Inc., New York, New York, 1960.

3. Stogryn, A., "A Note on Brighteness Temperature at Millimeter Wavelengths," IEEE Trans. on Geoscience Electronics, Vol. GE-13, No. 2, pp 81-84, April 1975.

4. Thaddeus, P., "The Short-Wavelength Spectrum of the Microwave Background," Annual Review of Astronomy and Astrophysics, Vol. 10, pp 305-334, 1972.

5. Rosenkranz, P. W., "Shape of the 5 mm Oxygen Band in the Atmosphere, *IEEE Trans. on Antennas and Propagation*, Vol. AP-23, No. 4, July 1975.

6. Gordon, R. G., "Semiclassical Theory of Spectra and Relaxation in Molecular Gasses," J. Chem. Phys., Vol. 45, pp 1649-1655, September 1, 1966.

7. Van Vleck, J. H., "Absorption of Microwaves by Oxygen," Physical Review, Vol. 71, pp 413-424, 1947.

8. Staelin, David H., "Measurements and Interpretation of the Microwave Spectrum of the Terrestrial Atmosphere near 1-Centimeter Wavelength," Journal of Geophysical Research, Vol. 71, pp 2875-2881, 1966.

9. Barrett, A. H. and Chung, V. K., "A Method for the Determination of High-Altitude Water-Vapor Abundance from Ground-Based Microwave Observations," Journal of Geophysical Research, Vol. 67, pp 4259-4266, 1962.

10. Van Vleck, J. H., "Absorption of Microwaves by Water Vapor," Physical Review, Vol. 71, pp 425-432, 1947.

11. Paris, J. F., "Transfer of Thermal Microwaves in the Atmosphere," Thesis, Department of Meteorology, Texas A&M, 1971.

12. Saxton, J. A. and Lane, J. A., "Electrical Properties of Sea Water," Wireless Engineer, p. 269, October 1952.

13. Hollinger, J. P., "Passive Microwave Measurements of Sea Surface Roughness," IEEE Trans. on Geoscience Electronics, Vol GE-9, pp 165-169, July 1971.

14. Hollinger, J. P. "Remote Passive Microwave Sensing of the Ocean Surface," Proc. Seventh International Symposium on Remote Sensing of EnvironmenVol. III, pp 1807-1817, May 1971.

15. Nordberg, W., Conaway, J., Ross, D. B., and Wilheit, T., "Measurements of Microwave Emission from a Foam-Covered Wind Driven Sea," J. Atmos. Sci., Vol. 28, pp 429-435, 1971.

16. Ross, D. B. and Cardone, V. J., "Observations of Oceanic Whitecaps and Their Relation to Remote Measurements of Surface Wind Speed," Journal of Geophysical Research, Vol. 79, pp 444-452, 1974.

17. Stogryn, A., "The Apparent Temperature of the Sea at Microwave Frequencies," IEEE Trans. on Antennas and Propagation, Vol. AP-15, pp 278-286, March 1967.

18. Wu, S. T., and Fung, A. K., "A Noncoherent Model for Microwave Emission and Backscattering from the Sea Surface," Journal of Geophysical Research, Vol. 77, No. 30, pp 5917-5929, October 1972.

19. Wagner, R. J. and Lynch, P. J., "Analytical Study of Microwave Sea Brightness Temperatures: A Composite Surface Model, " Report 17608-6010-RU-00, TRW Systems Group, Redondo Beach, California, December 1972.

20. Wentz, F. J., "A Two-Scale Scattering Model for Foam-Free Sea Microwave Brightness Temperatures," Journal of Geophysical Research, Vol. 80, No. 24, pp 3441-3446, August 1975.

21. Wait, J. R., "Electromagnetic Waves in Stratified Media," Pergamon Press, 1970.

22. Kraus, John D., "Radio Astronomy," McGraw-Hill Book Company, New York, New York, 1966.